Validation of IASI satellite ammonia observations at the pixel scale using in situ vertical profiles

Xuehui Guo, Lieven Clarisse, Rui Wang, Martin van Damme, Simon Whitburn, Pierre-François Coheur, Cathy Clerbaux, Bruno Franco, Da Pan, Levi M. Golston, et al.

1 **Validation of IASI satellite ammonia observations at the pixel scale using in-**
2 **situ vertical profiles**

3 Xuehui Guo[1], Lieven Clarisse[2], Rui Wang[1], Martin Van Damme[2], Simon Whitburn[2],
4 Pierre-François Coheur[2], Cathy Clerbaux[2,3], Bruno Franco[2], Da Pan[1], Levi M. Golston[1,4†],
5 Lars Wendt[5], Kang Sun[1,6†], Lei Tao[1,7], David Miller[1], Tomas Mikoviny[8,9,10†], Markus
6 Müller[11,12†], Armin Wisthaler[11,10], Alexandra G. Tevlin[13,14†], Jennifer G. Murphy[13], John B.
7 Nowak[15,16†], Joseph R. Roscioli[15], Rainer Volkamer[17,18,19], Natalie Kille[17,18,19], J. Andrew
8 Neuman[18,20], Scott J. Eilerman[21], James H. Crawford[16], Tara I. Yacovitch[15], John D.
9 Barrick[16], Amy Jo Scarino[16], and Mark A. Zondlo[1*]

10 [1]Department of Civil and Environmental Engineering, Princeton University, Princeton, NJ, USA

11 [2]Université libre de Bruxelles (ULB), Spectroscopy, Quantum Chemistry and Atmospheric
12 Remote Sensing (SQUARES), Brussels, Belgium

13 [3]LATMOS/IPSL, Sorbonne Université, UVSQ, CNRS, Paris, France

14 [4]Atmospheric Science Branch, NASA Ames Research Center, Moffett Field, CA, USA

15 [5]Hunterdon Central Regional High School, Flemington, NJ, USA

16 [6]Department of Civil, Structural and Environmental Engineering, University at Buffalo, Buffalo,
17 NY, USA

18 [7]Princeton Institute for the Science and Technology of Materials, Princeton, NJ, USA

19 [8]Chemistry and Dynamics Branch, Science Directorate, NASA Langley Research Center,
20 Hampton, VA, USA

21 [9]Oak Ridge Associated Universities, Oak Ridge, TN, USA

22 [10]Department of Chemistry, University of Oslo, Oslo, Norway

23 [11]Institute for Ion Physics and Applied Physics, University of Innsbruck, Innsbruck, Austria

24 [12]Ionicon Analytik, Innsbruck, Austria

25 [13]Department of Chemistry, University of Toronto, Toronto, Ontario, Canada

26 [14]Environment and Climate Change Canada, Toronto, ON, Canada

27 [15]Aerodyne Research Inc., Billerica, MA, USA

28 [16]NASA Langley Research Center, Hampton, VA, USA

29 [17]Department of Chemistry, University of Colorado Boulder, Boulder, CO, USA

30 [18]Cooperative Institute for Research in Environmental Sciences (CIRES), University of Colorado
31 Boulder, Boulder, CO, USA

32 [19]Department of Atmospheric Sciences, University of Colorado Boulder, Boulder, CO, USA

33 [20]NOAA Chemical Sciences Laboratory (CSL), Boulder, CO, USA

34 [21]Jupiter Intelligence, Boulder, Colorado 80302, USA

35 † - current affiliation

36 *Corresponding author: Mark A. Zondlo (mzondlo@princeton.edu)

37

Key Points:

- 39 IASI NH$_3$ columns agree well with those derived from boundary layer, in-situ
- 40 measurements with no significant biases at the pixel scale

- 41 Validation in a hotspot region shows best agreement at narrow spatiotemporal scales on
- 42 the order of the pixel size and mean wind speed

- 43 Additional accurate, airborne-based NH$_3$ datasets are critically needed for improved
- 44 validations across a range of environments

45

Abstract

47 Satellite ammonia (NH$_3$) observations provide unprecedented insights into NH$_3$
48 emissions, spatiotemporal variabilities and trends, but validation with in-situ measurements
49 remains lacking. Here, columns from the Infrared Atmospheric Sounding Interferometer (IASI)
50 were intercompared to boundary layer NH$_3$ profiles derived from aircraft- and surface-based
51 measurements primarily in Colorado, USA, in summer, 2014. IASI-NH$_3$ version 3 near real-time
52 dataset compared well to in-situ derived columns (windows $\pm$15 km around centroid, $\pm$1 hour
53 around overpass time) with good correlation (r=0.58), a slope near unity (0.78$\pm$0.14), and an
54 intercept of $2.1\times10^{15}\pm1.5\times10^{15}$ molec cm^{-2}. Agreement degrades at larger spatiotemporal
55 windows, consistent with the short atmospheric lifetime of NH$_3$. We also examined IASI version
56 3R, which relies on temperature retrievals from the ERA Reanalysis and a third product
57 generated using aircraft-measured temperature profiles. The overall agreements improve slightly
58 for both cases. Because no bias is observed within the combined measurement errors,
59 spatiotemporal averaging of IASI over large windows can be used to reduce retrieval noise.
60 Nonetheless, sampling artifacts of airborne NH$_3$ instruments result in significant uncertainties of
61 the in-situ-derived columns. For example, large validation differences exist between ascent and
62 descent profiles, and the assumptions of the free tropospheric NH$_3$ profiles used above the
63 aircraft ceiling significantly impact the validation. Because short-lived species like NH$_3$ largely
64 reside within the boundary layer with complex vertical structures, more comprehensive
65 validation is needed across a wide range of environments. More accurate and widespread in-situ
66 NH$_3$ datasets are therefore needed for improved validations of satellite products.

67

Plain Language Summary

69 Ammonia is an important species in the atmosphere that creates particulate pollution such as
70 haze, but it is challenging to measure especially from space. Major sources of ammonia include
71 agricultural activities. Improving our estimates of the emissions require widespread and frequent
72 measurements such as those from satellite. To date, satellite-based ammonia measurements have
73 not been extensively validated, particularly on the scale of individual measurements. We have
74 compared satellite ammonia measurements with those from ground-based and aircraft
75 measurements and show that satellite measurements are accurate at the pixel scale of an

76 individual measurement. However, we also show that it is important to consider the spatial and
77 temporal differences between the measurement scales (satellite vs. ground- and aircraft-based) in
78 regions where ammonia is concentrated, and large sources exist. Improved validations will
79 require advances in airborne ammonia measurement technologies, particularly for the relatively
80 low levels of ammonia that exist above the atmospheric boundary layer. Finally, additional
81 airborne-based measurements are needed to compare to satellite-based measurements in other
82 regions and seasons to extend these results more globally.

83

1. Introduction

85 Gas-phase ammonia (NH_3) is a ubiquitous base in the atmosphere and an important
86 component of the nitrogen cycle. Atmospheric NH_3 reacts with sulfuric acid and nitric acid to
87 form ammoniated (NH_4^+) aerosol particles, reducing visibility and causing adverse effects on
88 human health (Mensink & Deutsch, 2008; Ostro *et al.*, 2015; Wang *et al.*, 2006). Ammoniated
89 aerosols also affect the climate by scattering solar radiation, resulting in a negative radiative
90 forcing (IPCC, 2013). Excess NH_3 deposited to ecosystems can cause soil acidification, water
91 eutrophication and losses of biodiversity (Galloway *et al.*, 2004). Research suggests that NH_3
92 and NH_4^+ have become increasingly important in dry and wet deposition of reactive nitrogen (N_r)
93 in most parts of the United States due to reductions in nitrogen oxides (NO_x) emissions (Li *et al.*,
94 2016).

95 Agricultural activities such as fertilizer application and livestock waste management
96 contribute to over 80% of total NH_3 emissions globally (Bouwman *et al.*, 1997; Paulot *et al.*,
97 2014). Other anthropogenic sources of NH_3 include chemical production, residential waste and
98 vehicle emissions (Behera *et al.*, 2013; Sun *et al.*, 2017; Van Damme *et al.*, 2018). Global NH_3
99 emissions are expected to increase in the forthcoming decades due to growing food demands
100 (Erisman *et al.*, 2008; Lamarque *et al.*, 2011). NH_3 is unregulated in many countries, but active
101 efforts are being made to quantify NH_3 emissions and understanding their trends and
102 distributions on regional to global scales (Paulot *et al.*, 2014; Van Damme *et al.*, 2018). There
103 remain significant uncertainties in bottom-up NH_3 emission inventories as they require
104 representative measurements to scale from a small subset of sources to the entire global budget
105 (Beusen *et al.*, 2008; Golston *et al.*, 2020; Zhang *et al.*, 2018). On the other hand, top-down
106 approaches that depend on inverse modeling of NH_4^+ wet deposition data require widespread
107 observations, accurate vertical profiles, and chemical and deposition lifetimes (Paulot *et al.*,
108 2014; Zhu *et al.*, 2013). However, current major monitoring networks such as the Ammonia
109 Monitoring Network (AMoN) in the U.S. and the Nationwide Nitrogen Deposition Monitoring
110 Network (NNDMN) in China lack the spatial coverage and temporal resolution needed to fully
111 resolve the variabilities of NH_3, thereby introducing uncertainties in top-down estimates of NH_3
112 emissions (NADP, 2019; Xu *et al.*, 2015).

113 In the past decade, advances in remote sensing techniques have provided unprecedented
114 global coverage and medium-term time series for studying NH_3 on a broader scale not achievable
115 by ground-based measurements. Since the early 2000s, several satellites have been launched into
116 space with infrared sounders to measure atmospheric constituents. Examples of satellite NH_3
117 instruments are the Tropospheric Emission Spectrometer (TES) (Shephard *et al.*, 2011), Infrared
118 Atmospheric Sounding Interferometer (IASI) (Clarisse *et al.*, 2009; Van Damme *et al.*, 2017;
119 Whitburn *et al.*, 2016), Cross-track Infrared Sounder (CrIS) (Shephard & Cady-Pereira, 2015),

120 Atmospheric Infrared Sounder (AIRS) (Warner *et al.*, 2016) and Greenhouse Gases Observing
121 Satellite (GOSAT) (Someya *et al.*, 2019). Launched in 2004 and having ended its mission in
122 2018, TES provided the first satellite-based NH_3 product, though it only performed limited
123 measurements in its later years (Rasmussen, 2018). IASI provides Level-2 (L2) NH_3 products
124 dating back to 2008 with much broader spatial coverage than TES. AIRS has the longest data
125 record of NH_3 on a single satellite between 2002 and 2016 (Warner *et al.*, 2017). CrIS and
126 GOSAT are more recently developed NH_3 products with limited availability at this time
127 (Dammers *et al.*, 2019).

128 Despite the increasing use of satellite NH_3 products for inventory assessments, nitrogen
129 deposition, and aerosol chemistry, validations of satellite NH_3 measurements, especially those
130 against independent in-situ measurements, remain limited *(Dammers et al., 2019; Van Damme et*
131 *al.*, 2018; Zhang *et al.*, 2018). Although averaged satellite data over a large domain can be used
132 to study regional and global characteristics of NH_3, validations of individual satellite pixels help
133 further understand the capabilities and constraints of satellite observations. Meanwhile, analyses
134 of satellite NH_3 on fine temporal (e.g. daily and weekly) and local scales, such as fertilizer
135 emissions, require validation for increased confidence (Fortems-Cheiney *et al.*, 2016; Van
136 Damme *et al.*, 2018). Previously, Van Damme *et al.* (2015) used an averaged GEOS-Chem
137 model profile to convert IASI NH_3 columns into surface concentrations and found fair
138 agreements between IASI and ground-based observations on monthly scales, and moderate
139 correlations with hourly airborne data, but the fixed profile shapes used for the conversion
140 introduced certain biases in IASI surface concentration estimations. Dammers *et al.* (2016)
141 validated IASI using column measurements from ground-based high-resolution Fourier-
142 transform infrared spectroscopy (FTIR) at nine locations worldwide with spatial and temporal
143 windows of 25 km and 90 min, respectively. Good agreements (r ~ 0.8) were found where NH_3
144 levels were high, though the study removed outliers during wintertime. In addition, the FTIR
145 measurements themselves have not been validated by in-situ profiles and instead rely upon
146 model a priori and limited surface observations *(Dammers et al.*, 2015). Similarly, a comparison
147 between CrIS and FTIR was conducted by Dammers *et al.* (2017), where an overall good
148 correlation was observed, but the agreements for individual sites varied largely. Using a different
149 method, Sun *et al.* (2015) conducted a validation of TES NH_3 with collocated aircraft and mobile
150 lab measurements in California at the pixel scale and found the agreement to be within 10% for
151 selected dates. Furthermore, the spatial variability of NH_3 columns within a satellite pixel (IASI:
152 ~ 12 km in diameter) has been assessed over Colorado using structure functions analyses of
153 mobile NH_3 column observations conducted on fine spatial scales (few 10 meters; Follette-Cook
154 *et al.*, 2015; Kille *et al.*, 2017). During the time of this study, Kille *et al.* (2017) found 50% of
155 variability in NH_3 columns at distances less than approximately 1.6 km, and 90% of variability at
156 distances less than 6 km. The high atmospheric NH_3 variability poses a fundamental sampling
157 challenge to satellite validation on the pixel scale and illustrates the need for a multi-platform
158 sampling strategy for best results.

159 To expand the scope and robustness of satellite NH_3 validations, we compare the IASI
160 NH_3 at the pixel scale with a combination of aircraft-based profiles and an assortment of other
161 in-situ and mobile column surface observations taken during the summer of 2014 in Colorado,
162 USA, with some insight on the winter of 2013 in California, USA. The general approach used
163 here can be readily applied to other satellite NH_3 products, provided that NH_3 vertical profiles
164 are nearly collocated with the satellite pixels within a temporal window that is consistent with
165 wind and atmospheric transport.

166 **2. Data and Methods**

167   2.1. IASI Observations

168   IASI is an infrared sounder onboard the polar-orbiting Metop-A/B/C satellites, which
169 were respectively launched in 2006, 2012 and 2018 (Clerbaux *et al.*, 2009). It is sensitive to NH_3
170 absorption features mainly between 800 and 1200 cm^{-1} (Clarisse *et al.*, 2010; Coheur *et al.*,
171 2009). IASI provides twice-daily measurements of NH_3 with overpass times of 0930/2130 local
172 solar time (LST). IASI has a swath of 2400 km and a pixel size of 12 km in diameter at nadir.
173 The first IASI NH_3 product was retrieved using lookup tables (LUTs) based on simulations from
174 a forward radiative transfer model. A hyperspectral range index (HRI) was calculated from each
175 observation and converted to NH_3 columns using the LUTs (Van Damme *et al.*, 2014). A
176 subsequent version (ANNI-NH3-v1) improved the retrieval of NH_3 by using an artificial neural
177 network for IASI (ANNI) to transform the calculated HRI into column densities (Whitburn *et al.*,
178 2016). Version 2 of the ANNI product further improved the algorithm by introducing separate
179 neural networks for land and sea, and simplified input parameters. With the release of this
180 version, an additional product was made available using meteorological retrievals from the
181 European Centre for Medium-Range Weather Forecasts Re-Analysis (ERA)-Interim ECMWF
182 for better interannual consistency, as opposed to using meteorological data from IASI itself to
183 calculate columns (Van Damme *et al.*, 2017). It is emphasized that the ANNI-NH_3 products do
184 not produce information on averaging kernel (AVK) because the current retrieval method is not
185 based on optimal estimation (Whitburn *et al.*, 2016). Thus, only the unconstrained columns were
186 used here to provide an overview of the agreement between IASI and in-situ measurements.

187   In this work, we analyze version 3 of the ANNI-NH_3 product from IASI Metop-A/B. This
188 version, processed using the retrieval framework outlined in (Franco *et al.*, 2018), features a
189 slightly increased measurement sensitivity due to small changes in the neural network
190 architecture and training and improved post-filtering. In addition, several debiasing procedures
191 have been introduced to correct for the gradual increase of CO_2 columns over the entire IASI
192 time-period and for IASI instrument calibrations. Despite the significant number of changes from
193 v2 to v3, the changes to the retrieved columns are modest in the mean. For columns above
194 4×10^{15} molec cm^{-2}, 80% of the data agree to within 20%. As infrared retrievals are known to be
195 quite sensitive to auxiliary input data, we evaluate the following products: (1) The near real-time
196 product, retrieved using meteorological data from the European Organisation for the Exploitation
197 of Meteorological Satellites (EUMETSAT) with cloud coverage < 25%, (2) the reanalysis
198 product, retrieved using meteorological data from ERA5/ECMWF with cloud coverage < 10%,
199 and (3) a dedicated product retrieved using collocated in-situ temperature profiles from aircraft,
200 sonde and mobile measurements (other meteorological data such as skin temperature are from
201 EUMETSAT) with cloud coverage < 25%. We only include the morning observations over land
202 surfaces as IASI has better sensitivity to NH_3 under these conditions.

203   2.2. In-situ Measurements

204   The Deriving Information on Surface conditions from Column and Vertically Resolved
205 Observations Relevant to Air Quality (DISCOVER-AQ) field experiment was a multi-year
206 campaign led by the National Aeronautics and Space Administration (NASA) (Crawford &
207 Pickering, 2014). Its mission was to validate collocated satellite observations of atmospheric

208   pollutants over four regions in the U.S. (Baltimore/Washington, California, Houston, and
209   Colorado). Airborne NH_3 measurements were only available in the California and Colorado
210   campaigns, the foci of this study. The California campaign occurred between January 16 and
211   February 7, 2013 over the San Joaquin Valley. In the following year, the experiment was
212   continued in Colorado from July 16 to August 16, along with a complimentary National Science
213   Foundation (NSF) Front Range Air Pollution and Photochemistry Experiment (FRAPPÉ) that
214   had additional platforms and NH_3 measurements (Flocke *et al.*, 2020). The DISCOVER-AQ
215   flight patterns were specifically designed for satellite validations as the P-3B aircraft made
216   repeated upward and downward spirals at several designated locations for the construction of
217   vertical profiles. A typical P-3B spiral roughly spanned 5 km in diameter, which were
218   particularly advantageous for validations of short-lived species such as NH_3 that exhibits strong
219   spatial gradients near source regions.

220   A unique aspect of the 2014 Colorado campaign compared to past field experiments was
221   the comprehensive suite of NH_3 measurements on multiple platforms: two aircraft, a tall tower,
222   and four mobile laboratories. The NASA P-3B aircraft measured NH_3 with a proton-transfer
223   time-of-flight mass spectrometer (Müller *et al.*, 2014). The NSF/NCAR C-130 aircraft measured
224   NH_3 with a closed-path, quantum cascade laser-based instrument using a fast-response inertial
225   inlet to minimize sampling artifacts (QC-TILDAS, Aerodyne Research Inc.) (Schiferl *et al.*,
226   2016). A moving carriage on the Boulder Atmospheric Observatory's (BAO) 300 m tall tower in
227   Erie, Colorado made profiles every hour and was equipped with a closed-path, quantum cascade
228   laser-based NH_3 instrument (QC-TILDAS, Aerodyne Research Inc.) (Tevlin *et al.*, 2017). The
229   mobile laboratories included in-situ measurements from an open-path, quantum cascade laser-
230   based instrument onboard the Princeton Atmospheric Chemistry Experiment, a cavity ring down
231   instrument (Picarro G2103) onboard the NOAA Chemical Sciences Division (CSD) van, and a
232   closed-path, quantum cascade laser-based instrument (QC-TILDAS) on the Aerodyne Mobile
233   Laboratory (Eilerman *et al.*, 2016; Herndon *et al.*, 2005; Tao *et al.*, 2015). These three mobile
234   laboratories conducted a stationary and moving intercomparison and showed agreement to within
235   10% on average (Golston *et al.*, 2020). Column NH_3 abundances were measured by the
236   University of Colorado Solar Occultation Flux (CU SOF) instrument onboard the CU/NCAR
237   mobile laboratory (Kille *et al.*, 2017). CU SOF couples a digital fast solar tracker (Baidar *et al.*,
238   2016; Patent No. 10379194, 2019) to a fast scanning FTIR to measure the vertical column
239   integral of NH_3 and other gases above the mobile platform directly in the open atmosphere (Kille
240   *et al.*, 2017). Table 1 summarizes the performances of the NH_3 instruments during the two
241   campaigns.

242   In addition to the NH_3 measurements, temperature and pressure measurements were taken
243   from the P-3B aircraft and specially launched radiosondes (iMet-1 & Vaisala RS92) timed with
244   aircraft flights. These data allowed for the construction of in-situ derived NH_3 columns and for
245   the generation of IASI NH_3 measurements with in-situ temperature measurements as input. For
246   the determination of atmospheric mixed layer height (MLH) used in the construction of in-situ
247   NH_3 profiles, we examined P-3B aircraft profiles of other short-lived species with sources in this
248   region including nitrogen dioxide (NO_2) (Weinheimer *et al.*, 1994), ethane (C_2H_6) from gas-oil
249   activities (Yacovitch *et al.*, 2014), and the number concentration of particles (CN) with diameters
250   > 10 nm from the LARGE instrument (Beyersdorf *et al.*, 2016). Additional MLH measurements
251   were incorporated from the High Spectral Resolution LIDAR (HSRL2) instrument onboard the

252 NASA B200 aircraft (Scarino *et al.*, 2014). Table 2 lists the dates on which each platform was
253 functional during these campaigns.

Table 1. *Summary of in-situ NH₃ measurements during DISCOVER-AQ*

Platform	Method	Typical uncertainty	Referenced Work
California (2013)			
NASA P-3B aircraft	PTR-MS	± 35%	(Müller *et al.*, 2014)
NASA P-3B aircraft	CRDS	± (35% + 1.7 ppbv) + 0.2 ppbv[a]	(Schiferl *et al.*, 2016)
Princeton mobile	Open-path QCL	± 20%	(Miller *et al.*, 2015)
Colorado (2014)			
NASA P-3B aircraft	PTR-MS	± 35%	(Müller *et al.*, 2014)
NSF/NCAR C-130 aircraft	QC-TILDAS	± (22% + 0.305 ppbv) + 0.058 ppbv[a]	(Ellis *et al.*, 2010; Schiferl *et al.*, 2016)
Aerodyne mobile	QC-TILDAS	± (22% + 0.305 ppbv) + 0.058 ppbv[a]	(Ellis *et al.*, 2010; Schiferl *et al.*, 2016)
Princeton mobile	Open-path QCL	± 10% + 0.2 ppbv[a]	(Miller *et al.*, 2014; Tao *et al.*, 2015)
CU/NCAR mobile	SOF	± 4.4% + 1×10¹⁵ molec cm⁻² [a]	(Kille *et al.*, 2017)
NOAA CSD mobile	CRDS	± 20% + 1 ppbv[a]	(Eilerman *et al.*, 2016)
NOAA BAO tower	QC-TILDAS	± 20% + 0.5 ppbv[a]	(Tevlin *et al.*, 2017)

255 *Note.* PTR-MS = proton transfer reaction-mass spectrometer; CRDS = cavity ring down
256 spectrometer; QCL = quantum cascade laser; NSF = National Science Foundation; NCAR =
257 National Center for Atmospheric Research; QC-TILDAS = quantum cascade tunable infrared
258 laser direct/differential absorption spectroscopy; CU = University of Colorado; SOF = Solar
259 Occultation Flux. BAO = Boulder Atmospheric Observatory. Uncertainties are presented as
260 reported in archived field data catalog and/or related publications. Subscripts in the third column:
261 [a] uncertainty + limit of detection.

262 **Table 2.** *Availability of in-situ NH₃ measurements in DISCOVER-AQ California in 2013 (upper*
263 *table) and Colorado in 2014 (lower table). Colored and blank cells represent dates when data*
264 *from each platform were or were not available, respectively.*

Platform \ Date	1/16	1/17	1/18	1/19	1/20	1/21	1/22	1/25	1/26	1/27	1/28	1/29	1/30	1/31	2/1	2/3	2/4	2/5	2/6	2/7
NASA P-3B (PTR-MS, A.Wisthaler)	■		■		■	■	■						■	■	■		■		■	
NASA P-3B (CRDS, J. Nowak & A. Neuman)	■		■		■						■		■	■	■		■		■	
Princeton mobile (Open-path QCL, M. Zondlo)						■	■	■	■	■	■	■	■	■	■	■	■		■	■

7

265

Platform \ Date	7/16	7/17	7/18	7/19	7/20	7/21	7/22	7/23	7/24	7/25	7/26	7/27	7/28	7/29	7/30	7/31	8/1	8/2	8/3	8/4	8/5	8/6	8/7	8/8	8/9	8/10	8/11	8/12	8/13	8/14	8/15	8/16	8/18
NASA P-3B (PTR-MS, A.Wisthaler)		■			■	■	■	■				■	■	■		■						■	■	■		■							
NCAR/NSF C-130 (QC-TILDAS, S. Herndon, R. Roscioli, J. Nowak,)											■	■	■	■		■	■	■	■			■	■	■			■				■	■	■
Aerodyne mobile (QC-TILDAS, C. Floerchinger)	■	■	■		■		■			■	■	■	■	■	■	■	■	■	■	■	■	■	■	■	■	■	■	■	■				
Princeton mobile (Open-path QCL, M. Zondlo)	■			■	■	■	■			■	■	■		■		■		■	■		■		■	■		■		■	■				
CU mobile (SOF-FTIR, R. Volkamer)					■						■				■		■		■			■		■		■		■		■		■	■
NOAA CSD mobile (CRDS, A. Neuman)							■	■				■				■			■			■	■			■	■						
NOAA BAO tower (QC-TILDAS, J. Murphy)		■	■	■	■	■	■	■	■	■	■	■	■	■	■	■	■	■	■	■	■	■	■	■	■	■	■	■	■				

266   2.3. Validation Algorithm

267   2.3.1. Spatiotemporal filtering

268   The general framework of the validation algorithm used in this study is shown in Figure
269   1. For each valid IASI observation, we applied a spatiotemporal window centered on the pixel's
270   center location and overpass time to filter for DISCOVER-AQ data within the designated
271   window. For example, if an in-situ measurement was made inside a certain spatial distance (e.g.
272   ±15 km) from the center of the IASI pixel, and the time difference relative to the IASI overpass
273   time was within the temporal window (e.g. ±60 min), the measurement was considered valid for
274   comparison. This applied to all in-situ NH_3 measurements and other relevant data (e.g.
275   radiosondes). The only exception was the P-3B aircraft profiles, where we included all the data
276   in a vertical profile if the geographical center (mean latitude and longitude) of the aircraft spiral
277   fell inside the spatial window. Next, in-situ NH_3 measurements located within the spatiotemporal
278   window were aggregated into one dataset. Each collocation between IASI and in-situ
279   measurements required at least one aircraft profile available so that an NH_3 vertical profile could
280   be constructed. Figure 2 shows an example of collocation between IASI and in-situ
281   measurements on July 27, 2014. The location of IASI pixel centroid, denoted as a "+", is
282   positioned in the center with its footprint boundary outlined as a solid white ellipse. The spatial
283   window (in this case, ±15 km) is plotted as a dotted white circle. For demonstration purposes, the
284   ±3 hour temporal window is chosen to include as many measurements as possible. The route of
285   each in-situ platform is marked with a different color. In this example, in-situ NH_3 measurements
286   were available from P-3B, C-130, Princeton mobile lab and BAO tower.
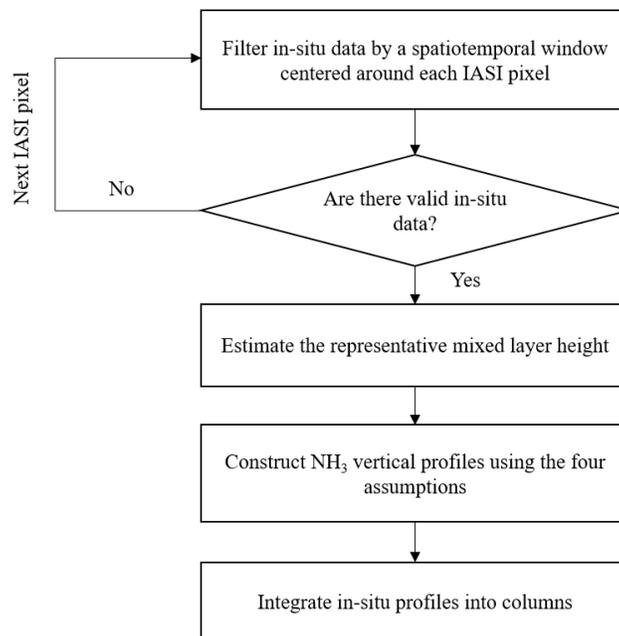
287

288 **Figure 1.** Overview of the validation algorithm. The flowchart is repeated for each valid IASI
289 pixel. If no in-situ data are found near the pixel, the pixel will be skipped, and the next available
290 pixel will be scanned for collocation. The four scenarios in box 4 are described in section 2.3.2
291 and illustrated with an example in Figure 3.

292

293
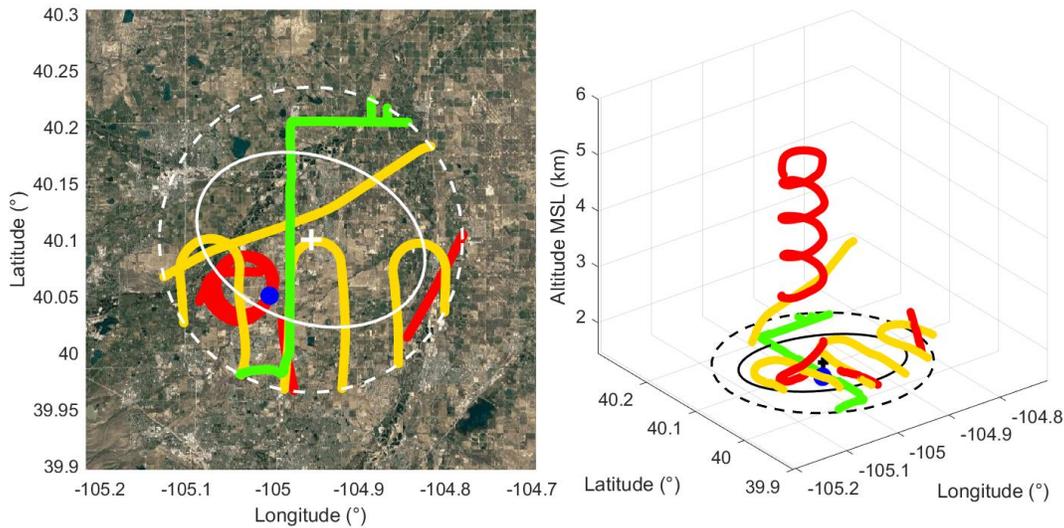
Figure 2. Example of collocated IASI and in-situ measurements on July 27, 2014 at 17:34:09 UTC. The left panel shows a two-dimensional view from the top and the right panel visualizes the movements of the in-situ platforms in a three-dimensional view. The center of the IASI pixel is denoted as "+". The solid ellipse marks the boundary of the IASI pixel. The dotted circle represents the ±15 km spatial window. The temporal window is ±3 hour in this case. Colored lines show the routes of the in-situ platforms: red = P-3B, yellow = C-130, green = Princeton mobile lab, blue dot = BAO tower. The 2D figure is overlaid on Google Maps (Google, Inc.) for better visualization of the geographical location and topography.

302   2.3.2. Reconciling uncertainties in NH_3 profiles

303   The combined in-situ dataset was then used to calculate the integrated column density of
304 NH_3. Two issues remained, however, in the construction of the in-situ-derived columns. First,
305 because the aircraft ceiling on most spirals was limited to ~ 5 km above sea level, it was
306 necessary to assume NH_3 concentrations in the middle and upper troposphere. Even though NH_3
307 is expected to accumulate mostly in the boundary layer because of its short-lifetime on the order
308 of hours to days (Dentener & Crutzen, 1994; Seinfeld & Pandis, 2016), NH_3 has been measured
309 in the middle and upper troposphere previously (Whitburn *et al.*, 2016). Höpfner *et al.* (2016) for
310 instance measured NH_3 levels in the upper troposphere to be tens of parts per trillion by volume
311 (1 pptv = 10^{-12} mol/mol) in the outflow of the active Monsoon system. However, the free
312 tropospheric NH_3 background was below the detection limit (< 3-5 pptv). More recently,
313 Höpfner *et al.* (2019) found that NH_3 concentrations in the upper troposphere could reach up to 1
314 ppbv in some regions during the Asian monsoon season, but were low in most other places.
315 Other studies that measured NH_3 profiles showed sharp decreases of NH_3 mixing ratio over
316 altitude (Nowak *et al.*, 2010), and low NH_3 (< 1 ppbv) at similar altitudes (Hoell *et al.*, 1980;
317 Ziereis & Arnold, 1986). Based on this evidence, it is reasonable to argue that NH_3
318 concentrations in the upper troposphere are negligible compared to the lower troposphere.
319 Second, a problem remained on how to deal with NH_3 concentrations measured by the aircraft
320 beyond the MLH. Previously, Sun *et al.* (2015) found that airborne NH_3 sensors (i.e. Picarro

321 CRDS and PTR-MS on the P-3B aircraft) in DISCOVER-AQ California exhibited sampling
322 artifacts above the MLH due to long and variable instrument response times. Because
323 DISCOVER-AQ CA and CO were in agricultural source regions, a strong gradient existed from
324 very high levels within the boundary layer to nominally-clean free tropospheric levels. Such
325 strong gradients can be problematic for accurately quantifying NH_3 with an instrument or inlet
326 that has a time response slower than the rapid changes in ambient mixing ratios (Fehsenfeld *et*
327 *al.*, 2002; Von Bobrutzki *et al.*, 2010).

328 Given these issues on the column construction from the aircraft data, we accounted for
329 the lack of a full tropospheric profile, and sampling artifacts, by bracketing four possible
330 scenarios of NH_3 distributions above the MLH in the troposphere. Figure 3 shows the case
331 studies used to address the vertical profile in the free troposphere: (1) integrating NH_3 only up to
332 the MLH, assuming negligible NH_3 concentrations above. Physically, this corresponds to the
333 assumption that NH_3 is contained within the boundary layer and dominates the column
334 measurement based on its short lifetime. It also assumes that sampling biases of instruments are
335 large in and around the strong gradient of the mixed layer. (2) Integrating NH_3 up to the
336 maximum aircraft altitude, assuming negligible NH_3 at altitudes higher than the aircraft ceiling.
337 This assumes that aircraft NH_3 measurements above the MLH are valid and real signals, but no
338 extrapolation is done beyond the aircraft range. (3) Integrating NH_3 up to the tropopause with
339 linear interpolation of decreasing mixing ratios from the maximum aircraft altitude to zero at the
340 tropopause estimated from sonde temperature profiles. In the real atmosphere, NH_3 is removed
341 from the atmosphere by reacting with nitric and sulfuric acids, and through dry deposition in the
342 gas phase and wet deposition as NH_4^+ by cloud scavenging (Mensink & Deutsch, 2008; Mizak *et*
343 *al.*, 2005; Nemitz, Milford, & Sutton, 2001). The linear interpolation represents a simplistic
344 mode of decay of NH_3 concentrations over altitude via the removal pathways. (4) Integrating
345 NH_3 up to the tropopause, while assuming constant NH_3 mixing ratio from the maximum aircraft
346 altitude to the tropopause. The last scenario features a well-mixed free troposphere in which NH_3
347 distributes uniformly in the vertical direction. In all four scenarios, we assumed NH_3 was
348 negligible further beyond the tropopause based on previous studies (Höpfner *et al.*, 2019, 2016).
349 While the truth is not likely to be any of these exact scenarios, these case studies of the free
350 tropospheric NH_3 distribution helped to bracket the magnitude and importance of the full NH_3
351 vertical profile that was not captured by the aircraft or caused by potential sampling problems in
352 the in-situ measurements.

353 Knowing the representative MLH for each collocation was necessary for the integration
354 of NH_3 profile in the first case. We estimated the MLH using three methods to minimize
355 potential errors and mismatches due to geographical elevation differences within the window: (1)
356 using the altitude of the first inversion of the temperature profile from the nearest timed sonde
357 launch (which may not necessarily be in the exact spatiotemporal window), (2) using aerosol
358 backscatter data from the B200 aircraft within the specified spatiotemporal window, and (3)
359 derived from the vertical profiles of other, short-lived atmospheric tracers (NO_2, C_2H_6 and CN >
360 10 nm) measured by P-3B. The final MLH was calculated as the average of all available methods
361 for each collocation.

362 2.3.3. Vertical integration

363   The available in-situ NH_3 measurements at 1 Hz were vertically binned every 100 m to
364   reduce noise, and the median value in each layer was used to build the final vertical profiles.
365   Median values were chosen because in-situ measurements on or near the ground immediately
366   downwind of sources (e.g. feedlots) would skew the mean to be unrepresentative of the overall
367   layer. When there was an altitude mismatch between the lowest in-situ bin and the ground at the
368   pixel's center location (i.e. in-situ altitude > IASI centroid altitude), the NH_3 mixing ratio at the
369   ground level was linearly extrapolated to the ground from the lowest bin. In cases where the
370   IASI centroid ground altitude was higher than in-situ locations, only measurements higher than
371   the ground altitude were included. Using the ideal gas law, the column NH_3 was integrated from
372   gas density over altitude:

373
$$\omega_{NH_3} = \int \frac{C_{NH_3} P_{air}}{k T_{air}} dz$$

374   where ω_{NH_3} is the column density of NH_3 in the same unit as IASI (molec cm^{-2}), C_{NH_3} is
375   the mixing ratio of NH_3 in air, P_{air} is the air pressure, k is the Boltzmann's constant, T_{air} is the
376   air temperature, and z is the altitude.
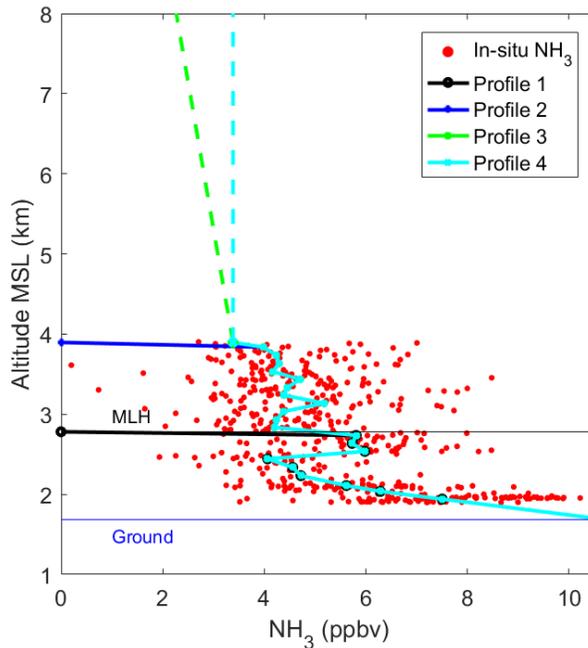
377

378   **Figure 3**. Four assumed NH_3 vertical profiles in this work. Profile 1 (black): integration up to
379   MLH with zero NH_3 above; Profile 2 (dark blue): integration up to maximum aircraft altitude
380   and zero NH_3 above; Profile 3 (green): integration up to tropopause with linear interpolation of
381   concentrations beyond aircraft altitudes to a value of zero at the tropopause; Profile 4 (turquoise):
382   integration up to tropopause assuming constant NH_3 beyond aircraft altitude. The median profile
383   from each assumption is shown with the interpolated sections above the aircraft altitude plotted
384   as dashed lines. In-situ NH_3 concentrations at 1 Hz are colored in red. The thin blue line

385 indicates the ground altitude at the IASI pixel center. The thin black line denotes the
386 corresponding MLH in this case. Altitude MSL stands for altitude above mean sea level.

387   The in-situ temperature profiles used for generating the alternative IASI-NH$_3$ product
388 described in section 2.1 were aggregated from the in-situ platforms in section 2.2 and filtered
389 using the spatiotemporal window of interest. Sonde measurements of temperature were needed to
390 fill in the gap of aircraft temperature measurements (e.g. near the ground, above the ceiling), yet
391 in many cases a sonde could not be found within the window. Therefore, we always used the
392 nearest sonde in time to construct the temperature profile, whether it was located within the
393 specified spatial window. In California, however, this approach was not ideal in winter. Due to
394 strong yet shallow inversions, there were often large discrepancies between the sonde
395 temperatures and those measured by the aircraft, especially near the surface. To reduce errors
396 due to separation in distance, we used P-3B aircraft temperatures where applicable and sonde
397 measurements outside the aircraft altitude range for California. In Colorado in summer, the
398 horizontal gradients of temperature were less pronounced, and temperature profiles measured by
399 P-3B and a given sonde usually matched up very well. Therefore, temperature data from the two
400 platforms were integrated together, while we further combined them with ground measurements
401 of temperature (e.g. mobile labs) if available. The merged temperatures were grouped in bins of
402 100 m, and the mean value in each bin was used to make the final temperature profile.

403   2.3.4. Data coverage

404   We quantify data coverage contributions from each in-situ platform to the validation
405 dataset using two approaches: (1) by the sum of total measurement time, and (2) by the number
406 of cases when the platform collocated with IASI. Some measurements were counted more than
407 once if they were found to collocate with IASI in multiple windows that we tested. Figure 4
408 shows that the P-3B aircraft that carried the PTR-MS instrument was the largest contributor to
409 the in-situ dataset in Colorado, because we required each IASI-in-situ collocation to have an
410 aircraft profile from P-3B (the C-130 aircraft, on the other hand, did not perform vertical profiles
411 at fixed locations). The Princeton mobile lab and the BAO tower were operational on most days
412 and became the next major contributors. Although each in-situ NH$_3$ instrument has a different
413 uncertainty estimate (Table 1), we applied a 30% error to the entire in-situ dataset to approximate
414 the overall instrument uncertainty. Because of potential systematic biases in the in-situ
415 measurements, we did not use a weighted average of errors from different measurements within
416 a given profile layer. Instrument biases were thought to be the limiting factors of the uncertainty
417 in all the in-situ measurements of NH$_3$ mixing ratio, and unlike random errors, these would not
418 be reduced through averaging.

419
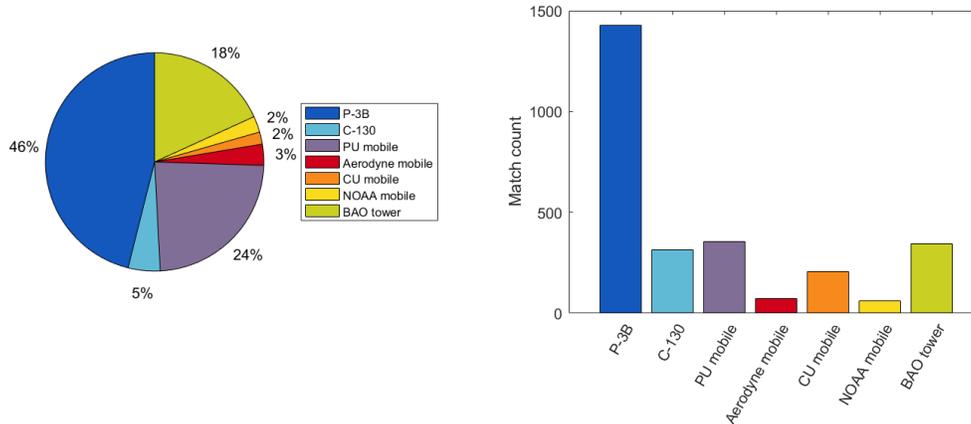
Figure 4. Data contribution from each in-situ platform in DISCOVER-AQ Colorado by (a) sum of total measurement time and (b) number of cases collocated with IASI. Statistics shown here are for all nine spatiotemporal windows tested in this study (total count of collocations = 1,426).

3. Results and Discussion

3.1. Comparison between Different In-situ Profiles

The four different scenarios of NH$_3$ profiles were quantitatively evaluated and compared based on the data in Colorado, given the larger suite of measurements in this campaign. For comparison purposes, we only show the comparison between in-situ and the reanalysis IASI product, but the overall conclusion holds true for the other two IASI products as well. The IASI reanalysis product versus the four in-situ profiles are plotted in Figure 5 with an orthogonal linear regression fit (MATLAB R2016b, MathWorks) that accounts for uncertainties in both the abscissa and ordinate variables. Profile 1 leads to the lowest column abundance among the four profiles because all the NH$_3$ measurements above the MLH are excluded. The column abundances increase sequentially from profile 1 to 4 as the contributions from the free troposphere increase. The correlation coefficient and slope between IASI and in-situ in Colorado indeed show a sequential degradation from profile 1 to 4 as extra NH$_3$ is added into the integration. We hypothesized in section 2.3 that the MLH assumption (profile 1) would be the closest representation of vertical distributions of NH$_3$ in the real atmosphere based on its short lifetime, emissions at the surface, and negligible amounts measured elsewhere in the free troposphere. Profile 1 shows the overall best agreement between IASI and in-situ, and this is consistent with the expectation that most NH$_3$ is accumulated within the boundary layer. We note that profile 2, which treats all aircraft data as valid, shows a similar correlation (though a factor of two difference in the slope). However, there are potential caveats associated with using the airborne measurements above the MLH given the sampling artifacts, which will be further discussed in section 3.5. All the correlations shown are tested to be statistically significant (p<0.05, same for all the analyses onward).

14
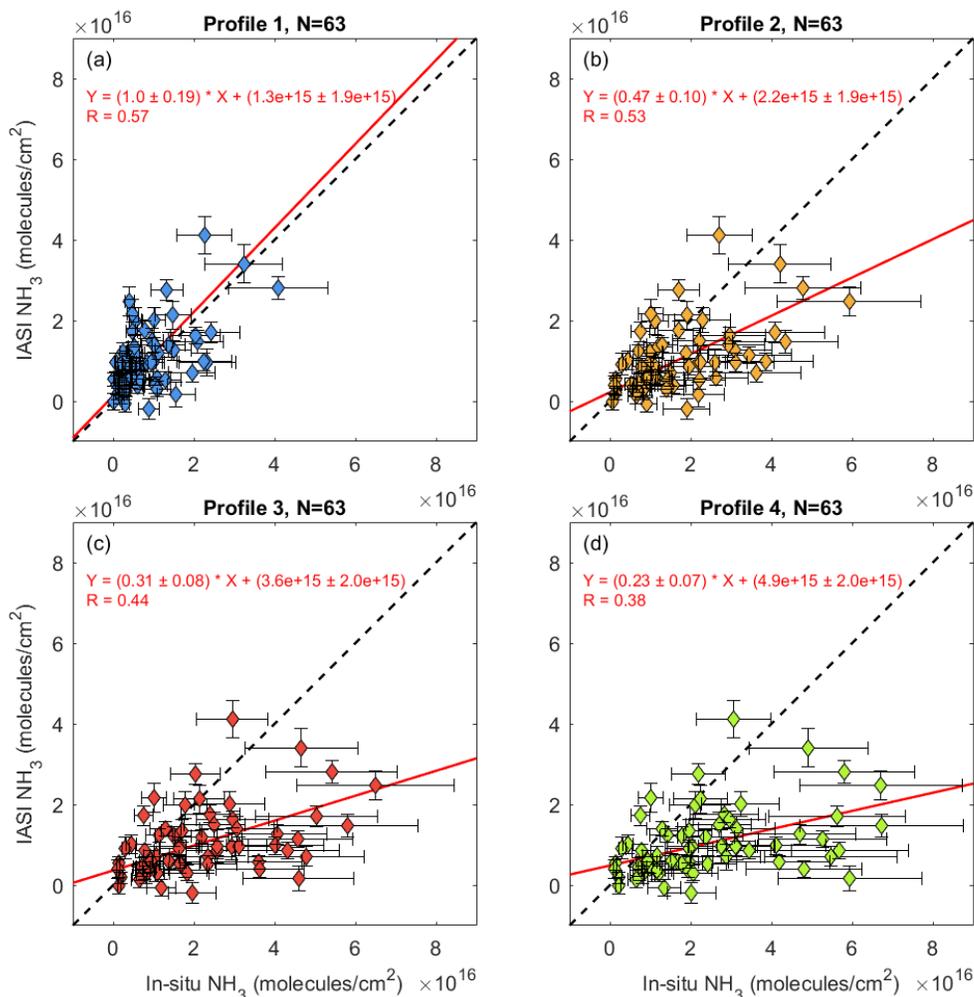
446

447 **Figure 5.** Reanalysis IASI product versus in-situ integrated columns from the four profiles for
448 the ±15 km and ±60 min in Colorado. Profile 1: integration up to MLH; Profile 2: integration up
449 to maximum aircraft altitude; Profile 3: integration up to tropopause assuming a linearly
450 decreasing NH_3 mixing ratio beyond aircraft altitude; Profile 4: integration up to tropopause
451 assuming constant NH_3 beyond aircraft altitude. Error bars indicate the uncertainties of columns.

452   3.2. Comparison between Different IASI Products

453   The three IASI products described in section 2.1 were compared with vertically
454 integrated in-situ columns under the MLH assumption (profile 1) within the ±15 km and ±60 min
455 window in Colorado (Fig. 6). We determined the optimal size of the spatiotemporal window
456 based on wind speeds in the boundary layer. To calculate typical boundary layer wind speeds, we
457 used wind data measured at 300 m on the BAO tower located in Erie, CO (40.050° N, 105.004°
458 W) from 0600-1200 local time during DISCOVER-AQ to bracket the IASI overpass times,
459 which are always in the morning. The average wind speed during the campaign was 3.5±2.2 m s⁻
460 ¹ (median: 3.1). The mean value is equivalent to a spatial window of approximately 15 km in
461 diameter on an hourly scale. While we recognize that wind conditions may vary slightly among
462 different regimes, we argue that a spatial window of ±15 km around the IASI centroids and a

15

463 temporal window ±60 min around the overpass times were internally consistent with one another
464 and can be used to account for the transport of NH_3 under typical atmospheric conditions during
465 this period.

466   The near real-time product comparing with in-situ columns integrated up to the MLH and
467 within the ±15 km and ±60 min spatiotemporal window yielded a correlation coefficient of 0.58,
468 an intercept of $2.1\pm1.5\times10^{15}$ molec cm^{-2} and a slope of 0.78±0.14. The reanalysis product
469 showed no real changes in the correlation coefficient (0.57) and intercept ($1.3\pm1.9\times10^{15}$ molec
470 cm^{-2}), but a slope closer to unity (1.0±0.19) was observed. The in-situ derived IASI product
471 showed a similar correlation (0.54), slope (1.1) and intercept ($1.7\pm2.2\times10^{15}$ molec cm^{-2}). All the
472 correlations are statistically significant. The intercepts for the three products are nearly
473 indistinguishable from zero, particularly when compared to column amounts $> 10^{16}$ molec cm^{-2},
474 suggesting that there is no significant absolute bias between the IASI and in-situ datasets.

475   Accurate temperature measurements are needed for NH_3 retrievals, especially in the
476 lower layers of the atmosphere where errors in the temperature profile can affect the retrieved
477 NH_3 columns significantly. The reanalysis product relies on gridded ECMWF meteorological
478 data, and our results showed the robustness of this implementation, which allows for long-term
479 consistent time series of IASI. The in-situ derived IASI product shows a slightly deviated slope
480 from unity, but the fact that this product matched well with the reanalysis product (Fig. 6d)
481 suggests that the retrievals are still internally coherent. The deviation may be attributed to the
482 fact that the in-situ temperature profiles largely consisted of sonde data, and sonde measurements
483 were not always representative of the IASI pixel in space and time. Our results are also
484 consistent with previous findings that the historic near real-time product (before the May 4, 2016
485 and the release of the IASI L2 version 6.2 by EUMETSAT) has a low bias against the reanalysis
486 product in version 2.1 of IASI NH_3 due an underestimation of the thermal contrasts between the
487 surface and the air at the altitude of interest (Van Damme *et al.*, 2017). The differences in
488 temperature inputs are further illustrated in Figure 7, where we plot the mean temperature profile
489 used in the retrieval of each IASI product (left panel) and an example of a single observation
490 (right panel). The different profile shapes and thermal contrast values explain why the retrieved
491 column abundances vary. The largest thermal contrast (TC, shown as inset) between the surface
492 temperature and skin temperature is found in the near real-time product, confirming the reason
493 why the retrieved columns are biased low against the other two products.

494
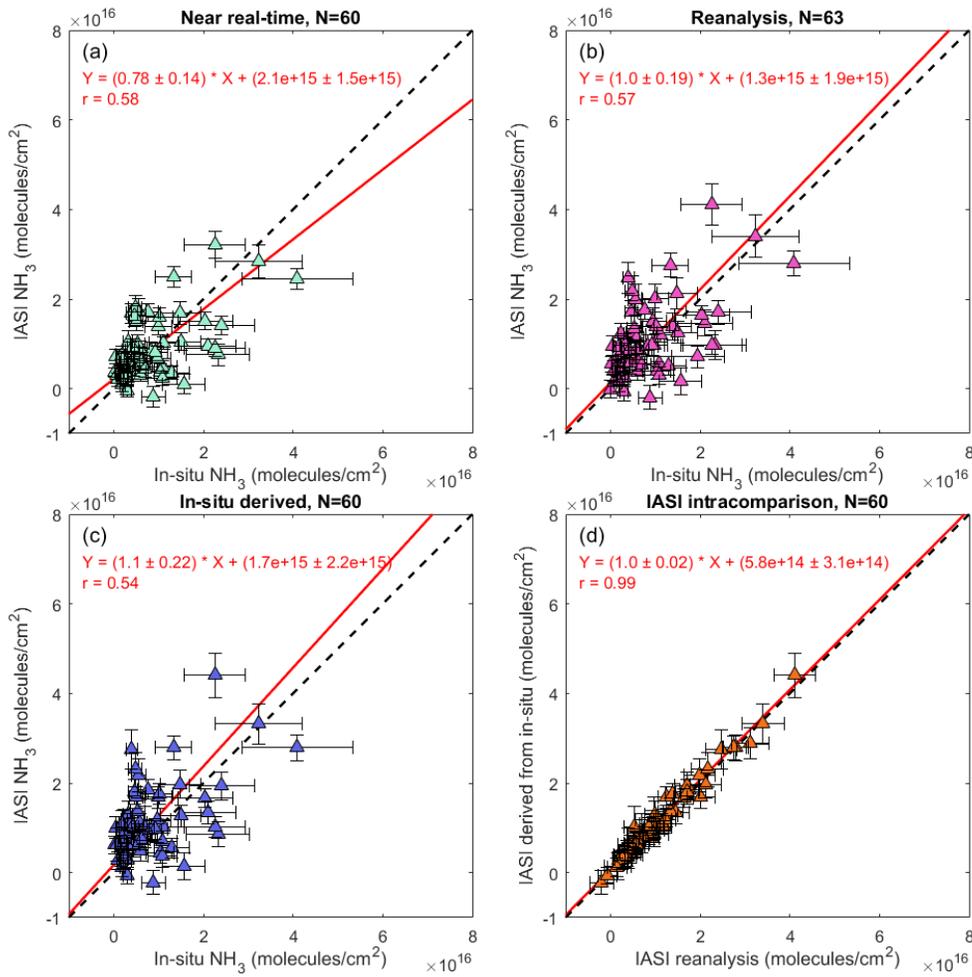
Figure 6. IASI-NH$_3$ products (a. near real-time, b. reanalysis, c. in-situ derived) versus the in-
situ NH$_3$ columns in Colorado based on the ±15 km and ±60 min window and MLH assumption.
The intracomparison between the reanalysis and in-situ derived IASI products is shown in (d).
Red line shows the best fit using orthogonal regression. Dashed line represents the 1:1 slope.

499
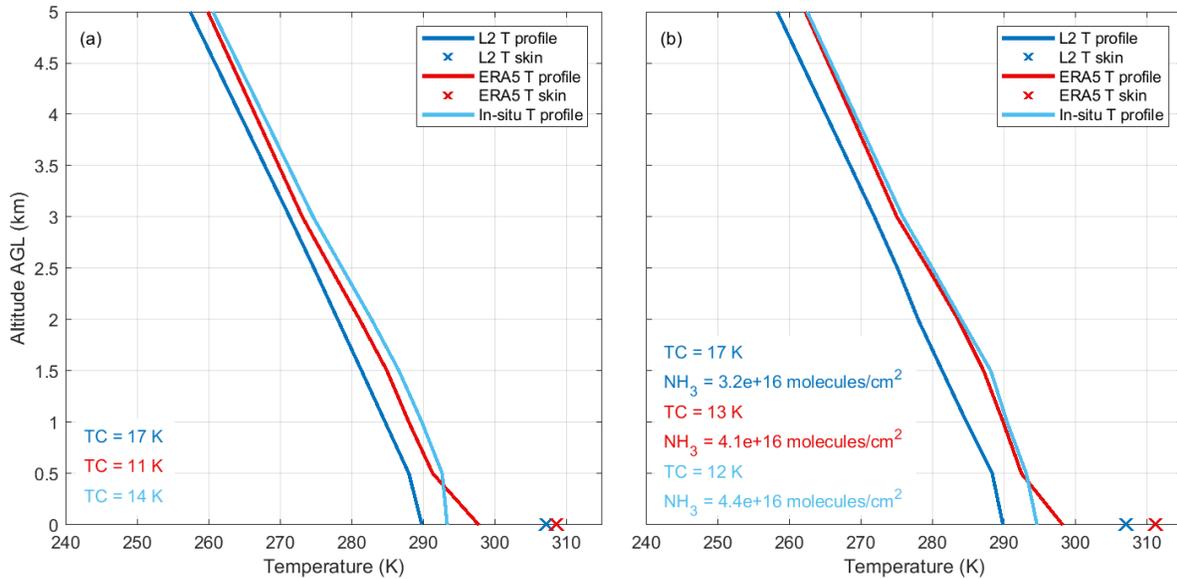
Figure 7. EUMETSAT L2 (dark blue), ERA5 (red) and in situ (light blue) temperature profiles used in the retrieval of near real-time, reanalysis and custom IASI products. Left panel: mean temperature profile in this study; right panel: a single observation on Aug 3, 2014 from IASI Metop-A (39.867° N, 105.205° W).

While linear regression provides a straightforward picture of how two datasets match with each other, the fitted slopes and intercepts can be driven by outliers on either side. We additionally calculated histograms to check for potential differences that may exist between the IASI and in-situ measurements. The remainders obtained from subtracting in-situ columns from corresponding IASI columns are illustrated in Figure 8 (same scenarios as Fig. 6: IASI products versus the in-situ MLH assumption for the ±15 km and ±60 min window in Colorado). The Freedman-Diaconis rule was used to calculate the appropriate bin width and number of bins for each distribution (Freedman & Diaconis, 1981). A Gaussian function was used to fit the remainders for a smoother interpretation of distribution. The histograms show that the remainders were clustered around zero for all three products, with the near real-time product having the smallest mean. This again indicates that the IASI products do not appear to have large systematic biases. Therefore, averaging IASI observations under different scenarios (low/moderate/high NH_3) likely will yield improved detection limits as any random measurement noise become averaged out.

518
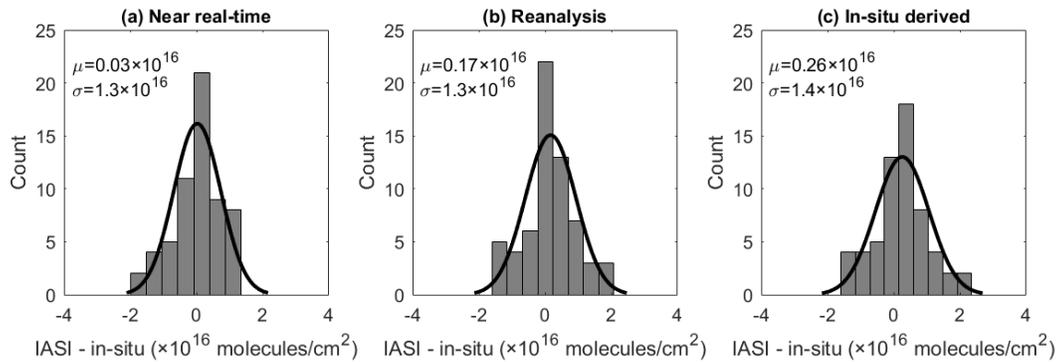
Figure 8. Histograms showing the remainders between IASI and in-situ NH$_3$ columns in Colorado (±15 km, ±60 min window, MLH assumption) for (a) the near real-time, (b) the reanalysis and (c) the in-situ derived products. The fitted Gaussian distribution is plotted as a black curve. μ and σ denote the mean and standard deviation of the fitted Gaussian function, respectively.

3.3. Comparison between Colorado and California

The DISCOVER-AQ California campaign was conducted over the San Joaquin Valley, the most productive agricultural region in the U.S., with Kern County and Tulare County ranking top in total value of production as of 2017 (CDFA, 2018). Previous studies have found significantly high NH$_3$ abundances in the San Joaquin Valley (Clarisse *et al.*, 2010; Makar *et al.*, 2009), making it a good area to evaluate the sensitivity of IASI towards surface NH$_3$. However, using the same criteria as for Colorado, only a limited number of collocated case (N=3, 9, 4 for near real-time, reanalysis and in-situ derived products) were found in California. Part of the reason was that only the Metop-A satellite was available during that time, whereas both MetOop-A and B were operational during the Colorado campaign. The main factor, however, was that the California campaign happened during winter in a valley area, where high cloud coverage, low thermal contrast and strong but shallow temperature inversions were frequently present. These conditions pose a challenge for accurate satellite NH$_3$ retrievals from an infrared sounder. For demonstration purposes, a test was conducted from January 16 to February 7, 2013 to retrieve NH$_3$ columns for all IASI Metop-A pixels within the DISCOVER-AQ California domain. Using the near real-time product as an example, only 23% of pixels produced valid columns after cloud filtering ($< 25\%$), and another 14% were removed after accounting for the availability of skin temperature and applying post-filtering, a process that is used to remove erroneous retrievals (Van Damme *et al.*, 2017). In contrast, a similar test between July 17 and August 10, 2014 over the DISCOVER-AQ Colorado domain showed that 52% of the Metop-A and B pixels remained after the retrieval process. The limited sample size makes it extremely difficult to draw any conclusions on the agreement between IASI and in-situ measurements in California. Given this, the scope of this study is limited to Colorado. The California example highlights the fact that validation results in one area may not apply to another area, especially where the conditions are dramatically different for satellite observations. Indeed, the same location may have different seasonality in the validation due to differences in thermal contrast. Similar to the results in Colorado, the reanalysis product in California yielded more datapoints available because of the increased availability of temperature profiles by using gridded, interpolated model data.

552   3.4. Comparison Between Spatiotemporal Windows

553   As described in section 3.2, we used the ±15 km spatial window in conjunction with the
554   ±60 min temporal window to account for the transport of NH_3 based on the typical boundary
555   layer wind speed of 3.5±2.2 m s^{-1}. We also evaluated the agreement between IASI and in-situ
556   data using other combinations of spatiotemporal windows that may be relevant. For comparison
557   purposes, we examined windows up to a factor of three apart in space and time to investigate the
558   sensitivity of spatiotemporal windows on the outcomes. Table 3 lists the orthogonal regression
559   results between IASI and the in-situ MLH assumption under nine different spatiotemporal
560   windows. The near real-time IASI product is shown here as an example. The correlations in all
561   nine windows are tested to be statistically significant. Aside from the ±15 km and ±60 min
562   window that has been adopted throughout the analysis, the ±15 km and ±20 min window also
563   showed good performance. The "within pixel" and ±60 min window even outperforms the
564   original window in terms of slope and correlation, which is reasonable since we anticipate that
565   most NH_3 emitted will stay near their sources in a short time frame. However, it should be noted
566   that the ±15 km and ±60 min window has a much larger sample size than the two windows
567   above, providing higher statistical power. From a statistical perspective, none of the remaining
568   windows are comparable to the ones discussed in terms of overall agreement.

569   **Table 3.** *Orthogonal regression statistics between the near real-time IASI product and the in-situ*
570   *MLH assumption for all the spatiotemporal windows tested, including overlapping points*

Temporal window	20 min			60 min			180 min		
Spatial window	Within pixel	15 km	45 km	Within pixel	15 km	45 km	Within pixel	15 km	45 km
m	0.93 ±0.17	0.76 ±0.18	0.60 ±0.17	2.1 ±0.73	0.78 ±0.14	0.85 ±0.13	2.3 ±0.50	2.7 ±0.67	1.1 ±0.15
b	8.0e14 ±2.4e15	1.2e15 ±2.7e15	3.4e15 ±1.5e15	-4.6e15 ±5.1e15	2.1e15 ±1.5e15	1.3e15 ±1.0e15	-3.9e15 ±3.2e15	-7.9e15 ±4.4e15	6.2e14 ±9.2e14
r	0.84	0.68	0.28	0.50	0.58	0.38	0.64	0.41	0.41
N	12	22	150	25	60	245	32	81	258
IASI mean	1.1e16 ±9.7e15	1.1e16 ±9.2e15	8.3e15 ±6.9e15	9.2e15 ±7.6e15	8.8e15 ±7.1e15	7.1e15 ±6.4e15	9.4e15 ±7.8e15	9.2e15 ±8.0e15	6.6e15 ±5.7e15
In-situ mean	1.1e16 ±1.0e16	1.3e16 ±1.1e16	8.1e15 ±8.0e15	6.6e15 ±5.1e15	8.5e16 ±8.2e15	6.8e15 ±6.8e15	5.7e15 ±4.4e15	6.3e15 ±5.0e15	5.5e15 ±5.5e15

571   *Note.* "Within pixel" means that the in-situ measurements must be located within the actual IASI
572   pixel (~ 12 km in diameter). m = slope; b = y-intercept (x-axis = in-situ, y-axis = IASI); r =
573   Pearson's correlation coefficient; N = number of datapoints. Standard deviations are shown for
574   slopes, intercepts and means.

575   3.5. Ascent and Descent Aircraft Profiles

576   An earlier study on the validation of TES NH_3 suggested that the two airborne NH_3
577   sensors (PTR-MS and CRDS) in DISCOVER-AQ California exhibited hysteresis during
578   sampling (Sun *et al.*, 2015). Due to the sensors' relatively long response times, the measured

579   NH_3 concentrations showed long tails of decay when exiting the boundary layer into the free
580   troposphere. On the other hand, the sensors detected almost no NH_3 signals when descending
581   from the free troposphere until reaching the boundary layer, likely due to an extended portion of
582   outgassing in clean conditions prior to the descent. The Colorado campaign only had PTR-MS
583   onboard the P-3B aircraft, but we also examined the differences in validation using the ascent
584   and descent profiles. It is emphasized that NH_3 data were only a side product of the PTR-MS
585   measurements during DISCOVER-AQ. The instrument was primarily measuring volatile organic
586   compounds (VOCs) and thus not optimized for detecting NH_3 (high instrumental background
587   resulting in a poor detection limit, slow time response due to a ~2 m long inlet line).

588   As an example of the hysteresis in sampling, we selected two pairs of locations relatively
589   close to each other where aircraft profiling was conducted to minimize the influence of NH_3
590   gradients across the transect. Figure 9a shows the time series on July 23, 2014, of NH_3 for an
591   ascent profile at NREL (Golden), a high-altitude leg near 5.5 km MSL for 22 km (2.5 min) and
592   then a descent spiral profile near the BAO tower (near Erie). The second pair of profiles
593   consisted of an ascent at Denver (La Casa), another high-altitude segment at 5.5 km MSL for 26
594   km (3 min.), followed by a descent at Chatfield Park south of Denver. MLH was estimated from
595   the aircraft temperature profiles and found to be similar between these locations (difference
596   within 100 m). The geographical locations of the four sites are shown in Figure 9b.

597   Figure 9c and d show the vertical profiles of NH_3 for the near-adjacent ascent and descent
598   pairs. For comparison, Figure 9e and f show the same pairs of profiles for C_2H_6, a petrochemical
599   tracer with a ~ 2 month lifetime that has sources located in the same general areas as NH_3
600   emissions in northeast Colorado and has no sampling issues (Kille *et al.*, 2019). The dashed line
601   marks the average boundary layer height averaged between each pair. For the first set of profiles
602   (Fig. 9c), the descent had an average NH_3 mixing ratio of 2.2 ppbv while the ascent averaged
603   over two times higher at 4.6 ppbv. We hypothesize these differences were mainly due to
604   instrument sampling issues because the corresponding C_2H_6 profiles (Fig. 9e) showed no
605   noticeable differences between the two sites, particularly the relative shapes of the profiles
606   around the MLH. This sampling hysteresis for NH_3 is consistent with those reported by Sun *et al.*
607   (2015). We investigated several other profiles and found similar patterns, especially when there
608   were large enhancements of NH_3 (> 5 ppbv) near the ground, suggesting that PTR-MS was
609   subject to artifacts caused by instrument design and sampling method as expected for any inlet-
610   based instrument.

611   For the second pair (Fig. 9d), the average NH_3 during descent again was lower than the
612   ascent, but there was a difference in air mass between these two sites. Figure 9f shows that C_2H_6
613   had different boundary layer profiles in the two locations, though were indistinguishable at and
614   above it. Nonetheless, the relative shapes of the NH_3 and C_2H_6 profiles are dramatically
615   different, with C_2H_6 showing an abrupt and large decrease above the MLH while NH_3 shows a
616   more gradual decrease around the MLH. The more gradual transition of NH_3 is again likely
617   related to sampling biases, though real air mass differences certainly play some role at least in
618   the boundary layer.
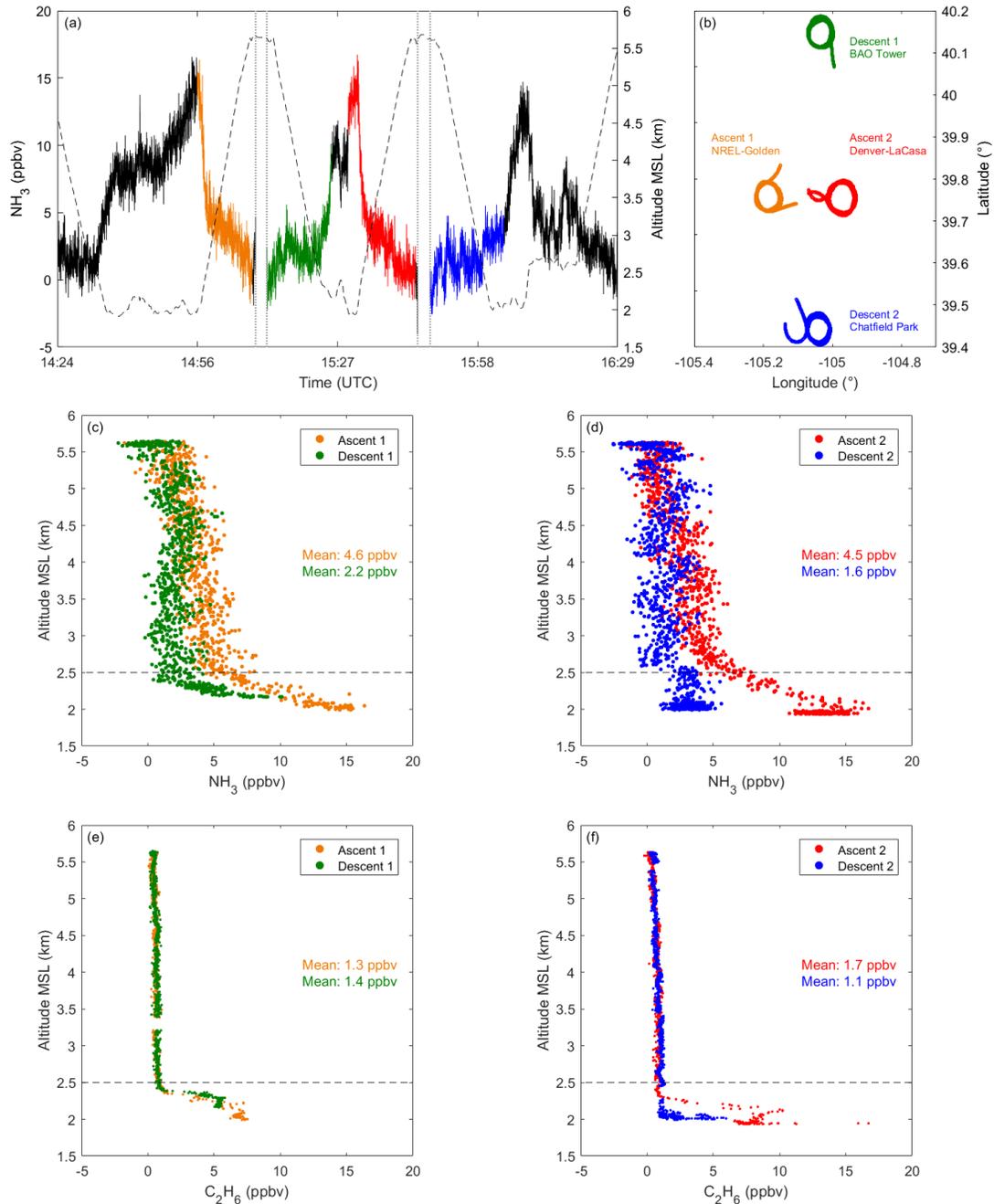
Figure 9. Vertical profiles of 1 Hz NH_3 and C_2H_6 measurements on the P-3B in Colorado on July 23, 2014. Panel (a) shows the time series of NH_3 measured by the PTR-MS. The two pairs of adjacent ascent and descent profiles selected for comparison are highlighted by different colors. The thin dashed line and grey dotted vertical lines show the altitude change during the flight and breaks in the time series, respectively. Panel (b) shows the geographical locations where the aircraft profiles were made. Panels (c) and (d) present the NH_3 profiles during the ascents and descents. Dashed lines mark the MLH averaged across each ascent and descent pair. Panels (e) and (f) are the corresponding C_2H_6 profiles measured simultaneously by a TILDAS instrument.

629   While we have demonstrated that IASI is comparable to in-situ-derived profiles in
630   general, the differences between ascent and descent profiles due to sampling issues require more
631   examination. To distinguish between ascent and descent aircraft profiles, we now compare the
632   three IASI products against ascents and descents separately (Fig. 10), and key differences are
633   readily observed. For example, the ascent profiles yield higher columns than corresponding IASI
634   columns, consistent with the above observations of instrument artifacts from outgassing.
635   Likewise, descent profiles are generally lower due to surface adsorption upon rapid increases in
636   NH_3 concentrations as one descends. As a result, descent clusters have higher slopes than the
637   ascent clusters. Descents tend to have much better correlations than ascents (0.62-0.68 vs. 0.43-
638   0.46) as well as slopes closer to unity, but their intercepts also tend to be worse. Because
639   sampling biases occur after large concentration changes regardless of the direction (net
640   adsorption vs. net outgassing), it is unclear which of these profiles is more representative of the
641   actual distribution. Therefore, we have opted to aggregate all PTR-MS measurements together
642   regardless of the flight direction. Our findings suggest that attention needs to be paid to the
643   discrepancies between ascent and descent profiles as a metric of in-situ, instrument
644   inlet/sampling performance. Future airborne research campaign targeting NH_3 concentrations
645   should employ sensors with highly quantified instrument responses in-flight, during upward and
646   downward flight profiles in the same location, and with high precisions and low biases for better
647   mapping of NH_3 vertical profiles.

648
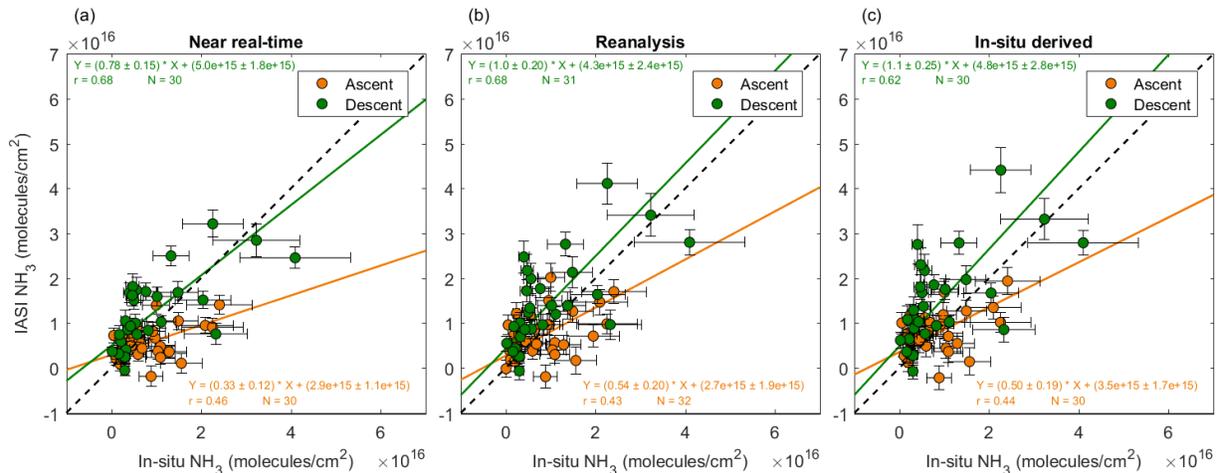
Figure 10. IASI-NH_3 products versus the in-situ NH_3 columns in Colorado ($\pm$15 km and $\pm$60
649   min window and MLH assumption) with ascent (orange) and descent (green) aircraft profiles
650   analyzed separately (same data as in Figure 6).
651

652   3.6. Comparison between IASI and CU SOF

653   Aside from in-situ NH_3 concentrations, ground-based mobile CU-SOF measurements of
654   NH_3 total columns were also available during the DISCOVER-AQ/FRAPPÉ Colorado campaign
655   (Kille *et al.*, 2017). We filtered the FTIR data using the same algorithm as the other in-situ
656   platforms but enlarged the window to $\pm$15 km and $\pm$180 min to include additional data that may
657   be potentially relevant. This was based on the variability of wind speed measured at BAO
658   (3.5 ± 2.2 m s^{-1}), where the $\pm$15 km and $\pm$180 min window is consistent with the lower boundary

659   of wind speed at 1σ standard deviation (1.3 m s^{-1}). For each collocation, the mean of all CU SOF
660   data within the window was computed. Figure 11 shows that IASI has moderate correlations
661   with FTIR, and the slopes are consistent with the 1:1 line. Given that FTIR retrievals depend
662   only weakly on a priori parameters (< 4% variation in column sensitivities), which also come
663   with large uncertainties (Kille *et al.*, 2019), this comparison shows some promising consistency
664   between the two instruments and independent approaches.
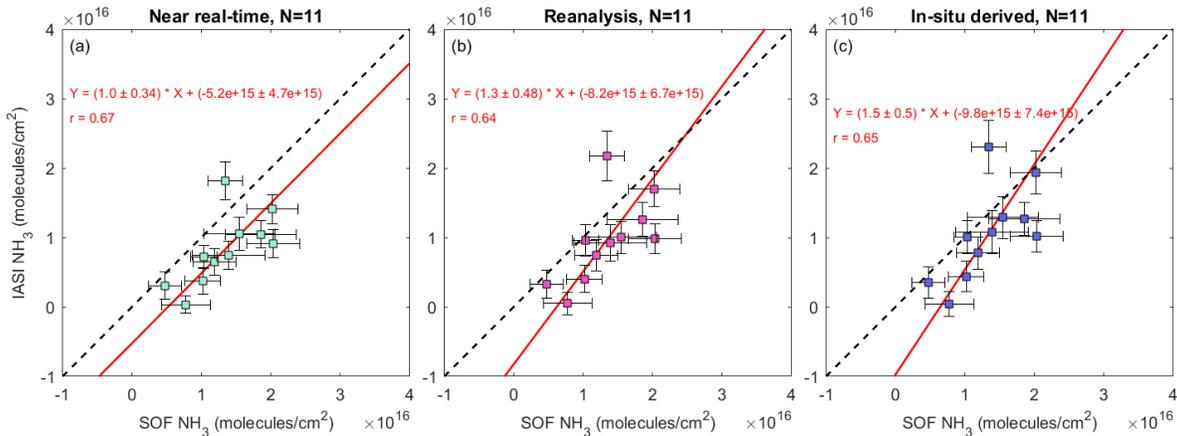
665

666   **Figure 11.** IASI versus CU SOF NH$_3$ columns using orthogonal regression for (a) the near real-
667   time, (b) the reanalysis, and (c) the in-situ derived products within the ±15 km and ±180 min
668   window in Colorado. All the correlations are statistically significant.

4. Implications

670   In the past decade, satellite NH$_3$ measurements have been used to study the trends and
671   distributions of NH$_3$ owing to their long data record and global coverage (Dammers et al., 2019;
672   Pinder et al., 2011; Van Damme et al., 2018; Warner et al., 2016). Although research has
673   attempted to validate satellite NH$_3$ using surface concentrations and ground-based stationary
674   FTIR measurements, the accuracies of localized measurements - which are important for
675   studying emission sources and their variabilities - have not been thoroughly validated. In this
676   work, we compared IASI with collocated in-situ-derived profiles and mobile SOF columns from
677   a suite of aircraft, tower, mobile laboratory, and sonde measurements from the NASA
678   DISCOVER-AQ and NSF FRAPPÉ field experiments. We validated version 3 of the IASI NH$_3$
679   dataset with three temperature profiles: the near real-time product from EUMETSAT, the
680   ERA5/ECMWF reanalysis product, and one using in-situ temperature profiles from the
681   DISCOVER-AQ/FRAPPÉ campaign.

682   IASI correlates well with in-situ NH$_3$ integrated up to the MLH within windows of ±15
683   km from the IASI centroid and ±60 min of the overpass time. The three IASI products show
684   similar performances, with the reanalysis product showing the overall best agreement (slope =
685   1.0±0.19, intercept = (1.3±1.9)×10^{15} molec cm^{-2}, r = 0.57). Because IASI has no significant
686   biases compared to the in-situ profiles, IASI columns can be spatiotemporally averaged for
687   improved signal to noise ratios where appropriate. The IASI retrieval depends on accurate
688   temperature inputs, especially in the boundary layer where most NH$_3$ resides. The near-real time

689 product showed a slight bias in the slope, which could be readily traced back to a known bias in
690 the IASI L2 temperature profile prior to 2016. Newer data do not exhibit such biases, with near-
691 real time and reanalysis products agreeing in the mean (Van Damme *et al.*, 2017). Limited
692 mobile CU SOF measurements during DISCOVER-AQ/FRAPPÉ Colorado also show overall
693 good consistency with IASI. Our IASI results are demonstrated for summer in Colorado USA
694 but may not be representative of other locations and times. More validations are needed,
695 especially in cases with strong inversions and low thermal contrast such as in valleys and in
696 winter. Large columns ($> 5 \times 10^{16}$ molec cm^{-2}) could also not be validated with the current set of
697 in situ measurements. We remind here that no AVK information was generated from IASI
698 retrievals or applied to the in-situ data, and therefore this study only presents a comparison
699 between the unbiased IASI columns and in-situ integrated columns. A weighting function is
700 being considered for future IASI versions that can be used to account for the variabilities of
701 vertical sensitivity.

702 This study is the first validation of IASI NH_3 at the single pixel scale using vertically
703 integrated in-situ concentrations. Nonetheless, as with TES single pixel validation results,
704 sampling artifacts of airborne NH_3 instruments remain a significant barrier for improved
705 validations. Not only are there fewer measurements of free tropospheric NH_3 from airborne
706 science field campaigns compared to other in-situ trace gases, but high accuracy and fast
707 response NH_3 measurements are critically needed for the mapping of NH_3 vertical profiles. This
708 is particularly important for validating in source regions where elevated concentrations in the
709 boundary layer may influence the corresponding free tropospheric values due to sampling biases
710 of existing instruments. Besides, vertical profiles of NH_3 in the boundary layer themselves have
711 complex structures due to emissions, partitioning into aerosol phases, and temperature and
712 relative humidity changes. More boundary layer NH_3 profiles will improve the development of
713 retrieval algorithms for all infrared sounders, and this can be achieved with recent advances in
714 NH_3 measurements techniques and the increased availability of airborne research campaigns
715 (Miller *et al.*, 2014; Pollack *et al.*, 2019).

716 Vertical profiles of NH_3 in the free troposphere are also a high priority, as the integrated
717 NH_3 concentrations in the free troposphere may be comparable to the overall column abundance
718 in low and moderate NH_3 locations. Spiral, vertical aircraft profiles like those made in
719 DISCOVER-AQ are critical for the validation of short-lived species like NH_3 such that
720 horizontal gradients are not manifested as vertical gradients during altitude changes. In addition,
721 repeated upward and downward transects over the same airmass will provide a measure of
722 confidence in any potential instrument sampling biases. While our study focuses on the
723 measurements from IASI, these generalized conclusions hold for all infrared sounders that are
724 sensitive to boundary layer temperature profiles and thermal contrast. Overall, more robust
725 datasets are needed for validating satellite NH_3 measurements, particularly at the pixel scale as
726 satellite NH_3 datasets are applied toward higher-resolution emission inventories and atmospheric
727 composition analyses.

Acknowledgments

765

Data Availability

767 All the datasets used in this work are publicly available and archived at the following websites:

768 DISCOVER-AQ/FRAPPÉ: https://www-air.larc.nasa.gov/missions/discover-aq/discover-aq.html

769 IASI: https://iasi.aeris-data.fr/NH3/

770

References

772 Baidar, S., Kille, N., Ortega, I., Sinreich, R., Thomson, D., Hannigan, J., & Volkamer, R. (2016).
773 Development of a digital mobile solar tracker. *Atmospheric Measurement Techniques*, *9*(3),

774   963–972. https://doi.org/10.5194/amt-9-963-2016

775   Behera, S. N., Sharma, M., Aneja, V. P., & Balasubramanian, R. (2013). Ammonia in the
776   atmosphere: A review on emission sources, atmospheric chemistry and deposition on
777   terrestrial bodies. *Environmental Science and Pollution Research*, *20*(11), 8092–8131.
778   https://doi.org/10.1007/s11356-013-2051-9

779   Beusen, A. H. W., Bouwman, A. F., Heuberger, P. S. C., Van Drecht, G., & Van Der Hoek, K.
780   W. (2008). Bottom-up uncertainty estimates of global ammonia emissions from global
781   agricultural production systems. *Atmospheric Environment*, *42*(24), 6067–6077.
782   https://doi.org/10.1016/j.atmosenv.2008.03.044

783   Beyersdorf, A. J., Ziemba, L. D., Chen, G., Corr, C. A., Crawford, J. H., Diskin, G. S., …
784   Anderson, B. E. (2016). The impacts of aerosol loading, composition, and water uptake on
785   aerosol extinction variability in the Baltimore-Washington, D.C. region. *Atmospheric
786   Chemistry and Physics*, *16*(2), 1003–1015. https://doi.org/10.5194/acp-16-1003-2016

787   Bouwman, A. F., Lee, D. S., Asman, W. A. H., Dentener, F. J., Hoek, K. W. Van Der, Olivier, J.
788   G. J., & Tg, N. (1997). A global high-resolution emission inventory for ammonia. *Global
789   Biogeochemical Cycles*, *11*(4), 561–587.

790   CDFA. (2018). *California Agricultural Statistics Review 2017-2018*. Retrieved from
791   www.cdfa.ca.gov/statistics

792   Clarisse, L., Clerbaux, C., Dentener, F., Hurtmans, D., & Coheur, P.-F. (2009). Global ammonia
793   distribution derived from infrared satellite observations. *Nature Geoscience*, *2*(7), 479–483.
794   https://doi.org/10.1038/ngeo551

795   Clarisse, L., Shephard, M. W., Dentener, F., Hurtmans, D., Cady-Pereira, K., Karagulian, F., …
796   Coheur, P. F. (2010). Satellite monitoring of ammonia: A case study of the San Joaquin
797   Valley. *Journal of Geophysical Research Atmospheres*, *115*(13), 1–15.
798   https://doi.org/10.1029/2009JD013291

799   Clerbaux, C., Boynard, A., Clarisse, L., George, M., Hadji-Lazaro, J., Herbin, H., … Coheur, P.-
800   F. (2009). Monitoring of atmospheric composition using the thermal infrared IASI/MetOp
801   sounder. *Atmospheric Chemistry and Physics*, *9*(16), 6041–6054.
802   https://doi.org/10.5194/acp-9-6041-2009

803   Coheur, P. F., Clarisse, L., Turquety, S., Hurtmans, D., & Clerbaux, C. (2009). IASI
804   measurements of reactive trace species in biomass burning plumes. *Atmospheric Chemistry
805   and Physics*, *9*(15), 5655–5667. https://doi.org/10.5194/acp-9-5655-2009

806   Crawford, J. H., & Pickering, K. E. (2014). DISCOVER-AQ: Advancing Strategies for Air
807   Quality Observations in the Next Decade. *Air & Waste Management Association*, 1–47.
808   Retrieved from https://www.awma.org/content.asp?admin=Y&contentid=301

809   Dammers, E., McLinden, C. A., Griffin, D., Shephard, M. W., Van Der Graaf, S., Lutsch, E., …
810   Erisman, J. W. (2019). NH3 emissions from large point sources derived from CrIS and IASI
811   satellite observations. *Atmospheric Chemistry and Physics*, *19*(19), 12261–12293.
812   https://doi.org/10.5194/acp-19-12261-2019

813   Dammers, E., Palm, M., Van Damme, M., Vigouroux, C., Smale, D., Conway, S., … Erisman, J.
814   W. (2016). An evaluation of IASI-NH3 with ground-based Fourier transform infrared

815   spectroscopy measurements. *Atmos. Chem. Phys*, *16*, 10351–10368.
816   https://doi.org/10.5194/acp-16-10351-2016

817 Dammers, E., Shephard, M. W., Palm, M., Cady-Pereira, K., Capps, S., Lutsch, E., … Willem
818   Erisman, J. (2017). Validation of the CrIS fast physical NH3 retrieval with ground-based
819   FTIR. *Atmospheric Measurement Techniques*, *10*(7), 2645–2667.
820   https://doi.org/10.5194/amt-10-2645-2017

821 Dammers, E., Vigouroux, C., Palm, M., Mahieu, E., Warneke, T., Smale, D., … Erisman, J. W.
822   (2015). Retrieval of ammonia from ground-based FTIR solar spectra. *Atmospheric*
823   *Chemistry and Physics Discussions*, *15*(16), 23279–23315. https://doi.org/10.5194/acpd-15-
824   23279-2015

825 Dentener, F. J., & Crutzen, P. J. (1994). A three-dimensional model of the global ammonia cycle.
826   *Journal of Atmospheric Chemistry*, *19*(4), 331–369. https://doi.org/10.1007/BF00694492

827 Eilerman, S. J., Peischl, J., Neuman, J. A., Ryerson, T. B., Aikin, K. C., Holloway, M. W., …
828   Herndon, S. (2016). Characterization of Ammonia, Methane, and Nitrous Oxide Emissions
829   from Concentrated Animal Feeding Operations in Northeastern Colorado. *Environmental*
830   *Science and Technology*, *50*(20), 10885–10893. https://doi.org/10.1021/acs.est.6b02851

831 Ellis, R. A., Murphy, J. G., Pattey, E., Van Haarlem, R., O'Brien, J. M., & Herndon, S. C.
832   (2010). Characterizing a Quantum Cascade Tunable Infrared Laser Differential Absorption
833   Spectrometer (QC-TILDAS) for measurements of atmospheric ammonia. *Atmospheric*
834   *Measurement Techniques*, *3*(2), 397–406. https://doi.org/10.5194/amt-3-397-2010

835 Erisman, J. W., Sutton, M. A., Galloway, J., Klimont, Z., & Winiwarter, W. (2008). How a
836   century of ammonia synthesis changed the world. *Nature Geoscience*, *1*(10), 636–639.
837   https://doi.org/10.1038/ngeo325

838 Fehsenfeld, F. C., Huey, L. G., Leibrock, E., Dissly, R., Williams, E., Ryerson, T. B., …
839   Hartsell, B. (2002). Results from an informal intercomparison of ammonia measurement
840   techniques. *Journal of Geophysical Research Atmospheres*, *107*(24), 1–15.
841   https://doi.org/10.1029/2001JD001327

842 Flocke, F., Pfister, G., Crawford, J. H., Pickering, K. E., Pierce, G., Bon, D., & Reddy, P. (2020).
843   Air Quality in the Northern Colorado Front Range Metro Area: The Front Range Air
844   Pollution and Photochemistry Éxperiment (FRAPPÉ). *Journal of Geophysical Research:*
845   *Atmospheres*, *125*(2). https://doi.org/10.1029/2019JD031197

846 Follette-Cook, M. B., Pickering, K. E., Crawford, J. H., Duncan, B. N., Loughner, C. P., Diskin,
847   G. S., … Weinheimer, A. J. (2015). Spatial and temporal variability of trace gas columns
848   derived from WRF/Chem regional model output: Planning for geostationary observations of
849   atmospheric composition. *Atmospheric Environment*, *118*, 28–44.
850   https://doi.org/10.1016/j.atmosenv.2015.07.024

851 Fortems-Cheiney, A., Dufour, G., Hamaoui-Laguel, L., Foret, G., Siour, G., Van Damme, M., …
852   Beekmann, M. (2016). Unaccounted variability in NH3 agricultural sources detected by
853   IASI contributing to European spring haze episode. *Geophysical Research Letters*, *43*(10),
854   5475–5482. https://doi.org/10.1002/2016GL069361

855 Franco, B., Clarisse, L., Stavrakou, T., Müller, J. F., Van Damme, M., Whitburn, S., … Coheur,
856   P. F. (2018). A General Framework for Global Retrievals of Trace Gases From IASI:

857   Application to Methanol, Formic Acid, and PAN. *Journal of Geophysical Research:*
858   *Atmospheres*, *123*(24), 13,963-13,984. https://doi.org/10.1029/2018JD029633

859 Freedman, D., & Diaconis, P. (1981). On the histogram as a density estimator:L2 theory.
860   *Zeitschrift Für Wahrscheinlichkeitstheorie Und Verwandte Gebiete*, *57*(4), 453–476.
861   https://doi.org/10.1007/BF01025868

862 Galloway, J. N., Dentener, F. J., Capone, D. G., Boyer, E. W., Howarth, R. W., Seitzinger, S. P.,
863   … Vöosmarty, C. J. (2004). Nitrogen Cycles: Past, Present, and Future. *Biogeochemistry*,
864   *70*(2), 153–226. https://doi.org/10.1007/s10533-004-0370-0

865 Golston, L. M., Pan, D., Sun, K., Tao, L., Zondlo, M. A., Eilerman, S. J., … Floerchinger, C.
866   (2020). Variability of ammonia and methane emissions from animal feeding operations in
867   northeastern Colorado. *Environmental Science and Technology*, es-2020-00301u.R1.

868 Herndon, S. C., Jayne, J. T., Zahniser, M. S., Worsnop, D. R., Knighton, B., Alwine, E., … Kolb,
869   C. E. (2005). Characterization of urban pollutant emission fluxes and ambient concentration
870   distributions using a mobile laboratory with rapid response instrumentation. *Faraday*
871   *Discussions*, *130*(0), 327–339. https://doi.org/10.1039/B500411J

872 Hoell, J. M., Harward, C. N., & Williams, B. S. (1980). Remote infrared heterodyne radiometer
873   measurements of atmospheric ammonia profiles. *Geophysical Research Letters*, *7*(5), 313–
874   316.

875 Höpfner, M., Ungermann, J., Borrmann, S., Wagner, R., Spang, R., Riese, M., … Wohltmann, I.
876   (2019). Ammonium nitrate particles formed in upper troposphere from ground ammonia
877   sources during Asian monsoons. *Nature Geoscience*, *12*(8), 608–612.
878   https://doi.org/10.1038/s41561-019-0385-8

879 Höpfner, M., Volkamer, R., Grabowski, U., Grutter, M., Orphal, J., Stiller, G., … Wetzel, G.
880   (2016). First detection of ammonia (NH3) in the Asian summer monsoon upper
881   troposphere. *Atmospheric Chemistry and Physics*, *16*(22), 14357–14369.
882   https://doi.org/10.5194/acp-16-14357-2016

883 IPCC. (2013). *Climate change 2013: The physical science basis, Intergovernmental Panel on*
884   *Climate Change (Ch. 8, p. 682)*. Cambridge, United Kingdom and New York, NY, USA:
885   Cambridge University Press.

886 Kille, N., Baidar, S., Handley, P., Ortega, I., Sinreich, R., Cooper, O. R., … Volkamer, R.
887   (2017). The CU mobile Solar Occultation Flux instrument: Structure functions and emission
888   rates of NH3, NO2 and C2H6. *Atmospheric Measurement Techniques*, *10*(1), 373–392.
889   https://doi.org/10.5194/amt-10-373-2017

890 Kille, N., Chiu, R., Frey, M., Hase, F., Sha, M. K., Blumenstock, T., … Volkamer, R. (2019).
891   Separation of Methane Emissions From Agricultural and Natural Gas Sources in the
892   Colorado Front Range. *Geophysical Research Letters*, *46*(7), 3990–3998.
893   https://doi.org/10.1029/2019GL082132

894 Lamarque, J. F., Kyle, P. P., Meinshausen, M., Riahi, K., Smith, S. J., van Vuuren, D. P., … Vitt,
895   F. (2011). Global and regional evolution of short-lived radiatively-active gases and aerosols
896   in the Representative Concentration Pathways. *Climatic Change*, *109*(1), 191–212.
897   https://doi.org/10.1007/s10584-011-0155-0

898 Li, Y., Schichtel, B. A., Walker, J. T., Schwede, D. B., Chen, X., Lehmann, C. M. B., … Collett,
899   J. L. (2016). Increasing importance of deposition of reduced nitrogen in the United States.
900   *Proceedings of the National Academy of Sciences of the United States of America*, *113*(21),
901   5874–5879. https://doi.org/10.1073/pnas.1525736113

902 Makar, P. A., Moran, M. D., Zheng, Q., Cousineau, S., Sassi, M., Duhamel, A., … Bouchet, V.
903   S. (2009). Modelling the impacts of ammonia emissions reductions on North American air
904   quality. *Atmospheric Chemistry and Physics*, *9*(18), 7183–7212.
905   https://doi.org/10.5194/acp-9-7183-2009

906 Mensink, C., & Deutsch, F. (2008). On the role of ammonia in the formation of PM2.5. *NATO*
907   *Science for Peace and Security Series C: Environmental Security*, 548–556.
908   https://doi.org/10.1007/978-1-4020-8453-9_60

909 Miller, D. J., Sun, K., Tao, L., Khan, M. a., & Zondlo, M. a. (2014). Open-path, quantum
910   cascade-laser-based sensor for high-resolution atmospheric ammonia measurements.
911   *Atmospheric Measurement Techniques*, *7*(1), 81–93. https://doi.org/10.5194/amt-7-81-2014

912 Miller, D. J., Sun, K., Tao, L., Zondlo, M. a., Nowak, J. B., Liu, Z., … Scarino, A. J. (2015).
913   Ammonia and methane dairy emission plumes in the San Joaquin Valley of California from
914   individual feedlot to regional scales. *Journal of Geophysical Research: Atmospheres*, n/a-
915   n/a. https://doi.org/10.1002/2015JD023241

916 Mizak, C. A., Campbell, S. W., Luther, M. E., Carnahan, R. P., Murphy, R. J., & Poor, N. D.
917   (2005). Below-cloud ammonia scavenging in convective thunderstorms at a coastal research
918   site in Tampa, FL, USA. *Atmospheric Environment*, *39*(9), 1575–1584.
919   https://doi.org/10.1016/j.atmosenv.2004.10.008

920 Müller, M., Mikoviny, T., Feil, S., Haidacher, S., Hanel, G., Hartungen, E., … Wisthaler, A.
921   (2014). A compact PTR-ToF-MS instrument for airborne measurements of volatile organic
922   compounds at high spatiotemporal resolution. *Atmospheric Measurement Techniques*,
923   *7*(11), 3763–3772. https://doi.org/10.5194/amt-7-3763-2014

924 National Atmospheric Deposition Program. (2019). Ammonia Monitoring Network (AMoN).
925   Retrieved from http://nadp.slh.wisc.edu/AMoN/

926 Nemitz, E., Milford, C., & Sutton, M. A. (2001). A two-layer canopy compensation point model
927   for describing bi-directional biosphere-atmosphere exchange of ammonia. *Quarterly*
928   *Journal of the Royal Meteorological Society*, *127*, 815–833.

929 Nowak, J. B., Neuman, J. A., Bahreini, R., Brock, C. A., Middlebrook, A. M., Wollny, A. G., …
930   Fehsenfeld, F. C. (2010). Airborne observations of ammonia and ammonium nitrate
931   formation over Houston, Texas. *Journal of Geophysical Research Atmospheres*, *115*(22), 1–
932   12. https://doi.org/10.1029/2010JD014195

933 Ostro, B., Hu, J., Goldberg, D., Reynolds, P., Hertz, A., Bernstein, L., & Kleeman, M. J. (2015).
934   Associations of mortality with long-term exposures to fine and ultrafine particles, species
935   and sources: results from the california teachers study cohort. *Environmental Health*
936   *Perspectives*, *123*(6), 549–556. https://doi.org/10.1289/ehp.1408565

937 Paulot, F., Jacob, D. J., Pinder, R. W., Bash, J. O., Travis, K., & Henze, D. K. (2014). Ammonia
938   emissions in the United States, European union, and China derived by high-resolution
939   inversion of ammonium wet deposition data: Interpretation with a new agricultural

940   emissions inventory (MASAGE_NH3). *Journal of Geophysical Research*, *119*(7), 4343–
941   4364. https://doi.org/10.1002/2013JD021130

942   Pinder, R. W., Walker, J. T., Bash, J. O., Cady-Pereira, K. E., Henze, D. K., Luo, M., …
943   Shephard, M. W. (2011). Quantifying spatial and seasonal variability in atmospheric
944   ammonia with in situ and space-based observations. *Geophysical Research Letters*, *38*(4),
945   1–5. https://doi.org/10.1029/2010GL046146

946   Pollack, I. B., Lindaas, J., Robert Roscioli, J., Agnese, M., Permar, W., Hu, L., & Fischer, E. V.
947   (2019). Evaluation of ambient ammonia measurements from a research aircraft using a
948   closed-path QC-TILDAS operated with active continuous passivation. *Atmospheric
949   Measurement Techniques*, *12*(7), 3717–3742. https://doi.org/10.5194/amt-12-3717-2019

950   Rasmussen, C. (2018). Farewell to a Pioneering Pollution Sensor. Retrieved June 3, 2020, from
951   NASA Jet Propulsion Laboratory website:
952   https://www.jpl.nasa.gov/news/news.php?feature=7061

953   Scarino, A. J., Obland, M. D., Fast, J. D., Burton, S. P., Ferrare, R. A., Hostetler, C. A., …
954   Harper, D. B. (2014). Comparison of mixed layer heights from airborne high spectral
955   resolution lidar, ground-based measurements, and the WRF-Chem model during CalNex
956   and CARES. *Atmospheric Chemistry and Physics*, *14*(11), 5547–5560.
957   https://doi.org/10.5194/acp-14-5547-2014

958   Schiferl, L. D., Heald, C. L., Damme, M. Van, Clarisse, L., Clerbaux, C., Coheur, P. F., …
959   Eilerman, S. J. (2016). Interannual variability of ammonia concentrations over the United
960   States: Sources and implications. *Atmospheric Chemistry and Physics*, *16*(18), 12305–
961   12328. https://doi.org/10.5194/acp-16-12305-2016

962   Seinfeld, J. H., & Pandis, S. N. (2016). *Atmospheric Chemistry and Physics: From Air Pollution
963   to Climate Change, 3rd Edition*. Hoboken, NJ: John Wiley & Sons.

964   Shephard, M. W., & Cady-Pereira, K. E. (2015). Cross-track Infrared Sounder (CrIS) satellite
965   observations of tropospheric ammonia. *Atmospheric Measurement Techniques*, *8*(3), 1323–
966   1336. https://doi.org/10.5194/amt-8-1323-2015

967   Shephard, M. W., Cady-Pereira, K. E., Luo, M., Henze, D. K., Pinder, R. W., Walker, J. T., …
968   Clarisse, L. (2011). TES ammonia retrieval strategy and global observations of the spatial
969   and seasonal variability of ammonia. *Atmospheric Chemistry and Physics*, *11*(20), 10743–
970   10763. https://doi.org/10.5194/acp-11-10743-2011

971   Someya, Y., Imasu, R., Shiomi, K., & Saitoh, N. (2019). Atmospheric ammonia retrieval from
972   the TANSO-FTS/GOSAT thermal infrared sounder. *Atmospheric Measurement Techniques
973   Discussions*, (April), 1–24. https://doi.org/10.5194/amt-2019-49

974   Sun, K., Cady-Pereira, K., Miller, D. J., Tao, L., Zondlo, M. A., Nowak, J. B., … Hostetler, C.
975   A. (2015). Validation of TES ammonia observations at the single pixel scale in the San
976   Joaquin Valley during DISCOVER-AQ. *Journal of Geophysical Research Atmospheres*,
977   *120*(10), 5140–5154. https://doi.org/10.1002/2014JD022846

978   Sun, K., Tao, L., Miller, D. J., Pan, D., Golston, L. M., Zondlo, M. A., … Zhu, T. (2017).
979   Vehicle Emissions as an Important Urban Ammonia Source in the United States and China.
980   *Environmental Science and Technology*, *51*(4), 2472–2481.
981   https://doi.org/10.1021/acs.est.6b02805

982 Tao, L., Sun, K., Miller, D. J., Pan, D., Golston, L. M., & Zondlo, M. a. (2015). Low-power,
983   open-path mobile sensing platform for high-resolution measurements of greenhouse gases
984   and air pollutants. *Applied Physics B*, 153–164. https://doi.org/10.1007/s00340-015-6069-1

985 Tevlin, A. G., Li, Y., Collett, J. L., McDuffie, E. E., Fischer, E. V., & Murphy, J. G. (2017). Tall
986   Tower Vertical Profiles and Diurnal Trends of Ammonia in the Colorado Front Range.
987   *Journal of Geophysical Research: Atmospheres*, *122*(22), 12,468-12,487.
988   https://doi.org/10.1002/2017JD026534

989 Van Damme, M., Clarisse, L., Dammers, E., Liu, X., Nowak, J. B., Clerbaux, C., … Coheur, P.
990   F. (2015). Towards validation of ammonia (NH3) measurements from the IASI satellite.
991   *Atmospheric Measurement Techniques*, *8*(3), 1575–1591. https://doi.org/10.5194/amt-8-
992   1575-2015

993 Van Damme, M., Clarisse, L., Heald, C. L., Hurtmans, D., Ngadi, Y., Clerbaux, C., … Coheur,
994   P. F. (2014). Global distributions, time series and error characterization of atmospheric
995   ammonia (NH3) from IASI satellite observations. *Atmospheric Chemistry and Physics*,
996   *14*(6), 2905–2922. https://doi.org/10.5194/acp-14-2905-2014

997 Van Damme, M., Clarisse, L., Whitburn, S., Hadji-Lazaro, J., Hurtmans, D., Clerbaux, C., &
998   Coheur, P. F. (2018). Industrial and agricultural ammonia point sources exposed. *Nature*,
999   *564*(7734), 99–103. https://doi.org/10.1038/s41586-018-0747-1

1000 Van Damme, M., Whitburn, S., Clarisse, L., Clerbaux, C., Hurtmans, D., & Coheur, P. F. (2017).
1001   Version 2 of the IASI NH3 neural network retrieval algorithm: Near-real-time and
1002   reanalysed datasets. *Atmospheric Measurement Techniques*, *10*(12), 4905–4914.
1003   https://doi.org/10.5194/amt-10-4905-2017

1004 Volkamer, R., Baidar, S., & Thomas, D. (2019). *Patent No. 10379194*. United States.

1005 Von Bobrutzki, K., Braban, C. F., Famulari, D., Jones, S. K., Blackall, T., Smith, T. E. L., …
1006   Nemitz, E. (2010). Field inter-comparison of eleven atmospheric ammonia measurement
1007   techniques. *Atmospheric Measurement Techniques*, *3*(1), 91–112.
1008   https://doi.org/10.5194/amt-3-91-2010

1009 Wang, J. L., Zhang, Y. H., Shao, M., & Liu, X. L. (2006). The quantitative relationship between
1010   visibility and mass concentration of PM2.5 in Beijing. *WIT Transactions on Ecology and
1011   the Environment*, *86*, 595–610. https://doi.org/10.2495/AIR06059

1012 Warner, J. X., Dickerson, R. R., Wei, Z., Strow, L. L., Wang, Y., & Liang, Q. (2017). Increased
1013   atmospheric ammonia over the world's major agricultural areas detected from space.
1014   *Geophysical Research Letters*, *44*(6), 2875–2884. https://doi.org/10.1002/2016GL072305

1015 Warner, J. X., Wei, Z., Larrabee Strow, L., Dickerson, R. R., & Nowak, J. B. (2016). The global
1016   tropospheric ammonia distribution as seen in the 13-year AIRS measurement record.
1017   *Atmospheric Chemistry and Physics*, *16*(8), 5467–5479. https://doi.org/10.5194/acp-16-
1018   5467-2016

1019 Weinheimer, A. J., Walega, J. G., Ridley, B. A., Gary, B. L., Blake, D. R., Blake, N. J., …
1020   Collins, J. E. (1994). Meridional distributions of NOx, NOy, and other species in the lower
1021   stratosphere and upper troposphere during AASE II. *Geophysical Research Letters*, *21*(23),
1022   2583–2586. https://doi.org/10.1029/94GL01897

Whitburn, S., Van Damme, M., Clarisse, L., Bauduin, S., Heald, C. L., Hadji-Lazaro, J., … Coheur, P.-F. (2016). A flexible and robust neural network IASI-NH3 retrieval algorithm. *Journal of Geophysical Research: Atmospheres*, *121*(11), 6581–6599. https://doi.org/10.1002/2016JD024828

Xu, W., Luo, X. S., Pan, Y. P., Zhang, L., Tang, A. H., Shen, J. L., … Liu, X. J. (2015). Quantifying atmospheric nitrogen deposition through a nationwide monitoring network across China. *Atmospheric Chemistry and Physics Discussions*, *15*(13), 18365–18405. https://doi.org/10.5194/acpd-15-18365-2015

Yacovitch, T. I., Herndon, S. C., Roscioli, J. R., Floerchinger, C., McGovern, R. M., Agnese, M., … Kolb, C. E. (2014). Demonstration of an ethane spectrometer for methane source identification. *Environmental Science and Technology*, *48*(14), 8028–8034. https://doi.org/10.1021/es501475q

Zhang, L., Chen, Y., Zhao, Y., Henze, D. K., Zhu, L., Song, Y., … Huang, B. (2018). Agricultural ammonia emissions in China: Reconciling bottom-up and top-down estimates. *Atmospheric Chemistry and Physics*, *18*(1), 339–355. https://doi.org/10.5194/acp-18-339-2018

Zhu, L., Henze, D. K., Cady-Pereira, K. E., Shephard, M. W., Luo, M., Pinder, R. W., … Jeong, G. R. (2013). Constraining U.S. ammonia emissions using TES remote sensing observations and the GEOS-Chem adjoint model. *Journal of Geophysical Research Atmospheres*, *118*(8), 3355–3368. https://doi.org/10.1002/jgrd.50166

Ziereis, H., & Arnold, F. (1986). Gaseous ammonia and ammonium ions in the free troposphere. *Nature*, 503–505.